Global and Planetary Change 171 (2018) 2–17

Contents lists available at ScienceDirect

Global and Planetary Change

journal homepage: www.elsevier.com/locate/gloplacha

Research article

The Arctic lithosphere: Thermo-mechanical structure and effective elastic thickness

Erzsébet L.M. Struijk[a], Magdala Tesauro[b,a,*], Nina N. Lebedeva-Ivanova[c], Carmen Gaina[c], Fred Beekman[a], Sierd A.P.L. Cloetingh[a]

[a] Department of Earth Sciences, Utrecht University, Netherlands
[b] Università di Trieste, Dipartimento di Matematica e Geoscienze, Italy
[c] Center for Earth Evolution and Dynamics, Department of Geosciences, University of Oslo, Norway

ARTICLE INFO

Keywords:
Arctic lithosphere
Thermal models
Lithospheric strength
Effective elastic thickness

ABSTRACT

For the first time, lithospheric temperatures, strength, and effective elastic thickness (*Te*) distributions are estimated for the Arctic region north of 68°. To this aim, we use ArcCRUST, a recent model of the Arctic crust, which includes the thickness and density of the crust and sediments, the boundaries between the continental and oceanic crust, and the age of the oceanic lithosphere. We estimate the temperature variations in the continental lithosphere assuming steady-state conditions, for a constant surface heat flow of 50 mWm^{-2} and 62 mWm^{-2} for the onshore and offshore regions, respectively. In the oceanic domain, the temperature variations are estimated adopting a global depth and heat flow model. We discuss the robustness of the results by comparing the new thermal field with temperatures obtained from inversion of a regional seismic velocity model. The results are used as input for estimating integrated strength and *Te*, assuming a mafic crustal rheology. Our models predict a sharp transition between cratonic areas, characterized by high strength and *Te*, and tectonically active areas with a weaker lithosphere, corresponding to the continental shelves and the oceanic spreading ridges. The significant lateral change in our modeled strength and *Te* at the edges of Greenland and Canadian Arctic and along the active mid-ocean ridge in the NE Atlantic corresponds to increased observed seismic activity.

1. Introduction

Lithospheric strength variations govern the long-term stability of tectonic features (e.g., Burov, 2011; François et al., 2013; Cloetingh et al., 2013; Cloetingh and Haq, 2015). The lithosphere of the Arctic region and its main continental and oceanic features have been partly investigated by seismic, gravity, and magnetic methods complemented by geological observations (e.g., Breivik et al., 2002; Franke et al., 2004; Gaina et al., 2011; Nikishin et al., 2014; Petrov et al., 2016). Various factors contribute to the present-day strength of the lithosphere, including lithospheric thermo-compositional variations and the presence of inherited structures from earlier tectonic episodes. The scarcity of direct observations, due to critical environmental conditions of the region, limits our knowledge on the structure and tectonic evolution of the Arctic. As a result, significant questions remain open regarding the present-day strength distribution in the Arctic lithosphere.

These questions are addressed in this study, in which we estimate the temperature, strength, and effective elastic thickness (*Te*) distribution of the Arctic lithosphere north of 68°, in order to map the first-order thermo-mechanical structure of its key tectonic features. For this purpose, we first use the new Arctic crustal model of Lebedeva-Ivanova et al. (2018) to estimate lithospheric thermal structure, assuming steady-state conditions in continental areas and using a plate model in the oceanic realm. The new thermal model is then compared with temperatures obtained from inversion of the seismic velocity model of Yakovlev et al. (2012) in order to assess the robustness of the approaches and assumptions used. The crustal and thermal models of the lithosphere are input for strength and *Te* estimates. Finally, we analyse the results obtained through a comparison with the seismicity distribution.

2. Tectonic setting

The Arctic lithosphere encompasses a range of tectonic domains of various age and composition (Fig. 1a–b). Cratonic cores of Archean and Proterozoic age are preserved in Greenland, the Canadian Arctic Islands, Siberia, and Scandinavia (e.g., Pease et al., 2014; Artemieva and Thybo, 2013). In the Paleozoic, important tectonic deformation phases

* Corresponding author.
E-mail address: mtesauro@units.it (M. Tesauro).

https://doi.org/10.1016/j.gloplacha.2018.07.014
Received 21 April 2017; Received in revised form 23 July 2018; Accepted 24 July 2018
Available online 29 July 2018
0921-8181/

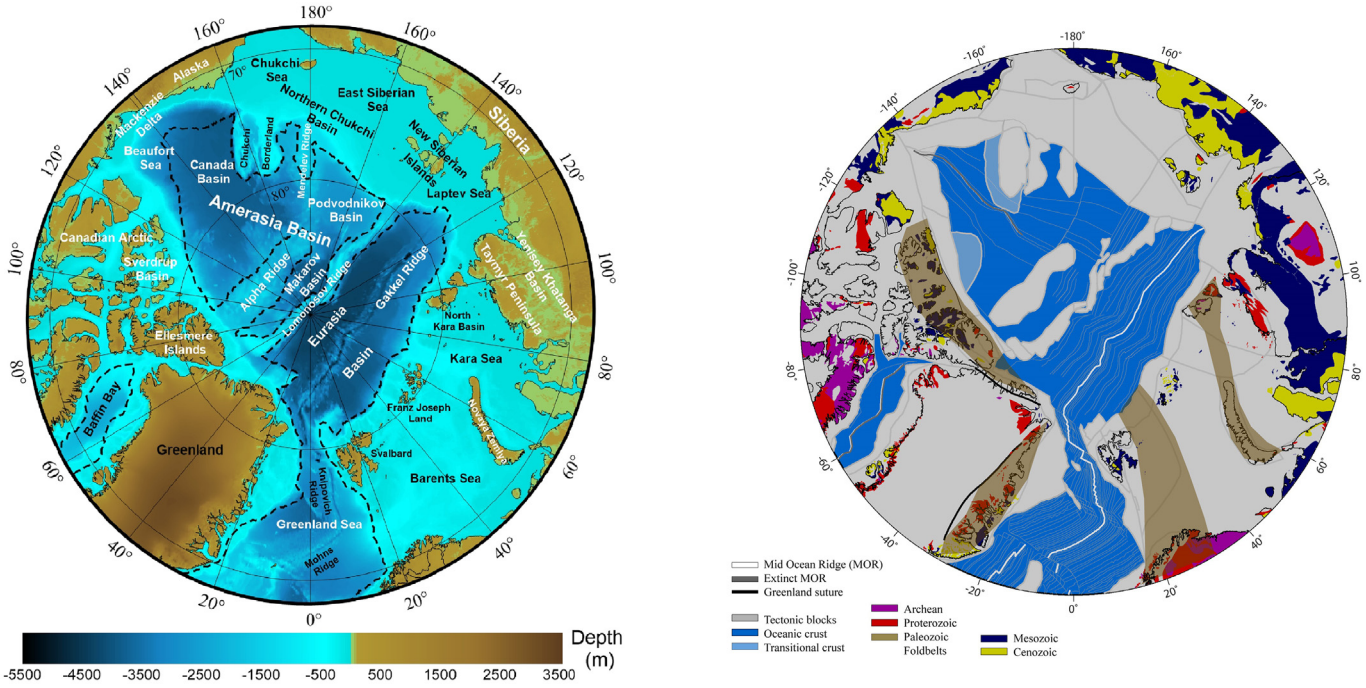

Fig. 1. (a) Topography and bathymetry map of the Circum-Arctic (after Jakobsson et al., 2012) in an orthographic projection including a model for the ocean-continent boundary (dashed black line). Although wide transitional regions between continental and oceanic lithosphere have been identified in several places of the Arctic, for simplicity reasons, we have depicted continent-ocean boundaries as dashed black lines and not wider transitional zones. (b) Arctic main tectonic provinces and simplified onshore geology. Tectonic blocks mark crustal independent blocks that moved relative to each other in geological time. Grey thin lines in the oceanic domains are isochrones inferred from geophysical data.

resulted from the convergence of the Laurentian and Baltic blocks and adjacent microcontinents and island arcs (e.g., Domeier, 2016) which created several orogenic belts (Caledonian – ca. 430 Ma, Ellesemerian - ca. 360 Ma, Uralian-Permo-Carboniferous - ca. 300 Ma). Part of the vast, shallow, extended shelves, like the Barents, Kara basins and part of the East Siberian shelf (Fig. 1b), were subjected to subsidence since the Paleozoic, which resulted in the formation of thick sedimentary successions (Johansen et al., 1993; Faleide et al., 2015).

Location of continental rift initiation is often controlled by pre-existing suture zones representing major rheological heterogeneities in the lithosphere (e.g., Smit et al., 2016 and Smit et al., 2018). Subduction along the Alaska (North Slope block) and Chukotka-East Siberian Shelf southern margins initiated rifting and extension in the northern margin of North America and the formation of various basins and isolated blocks in the Amerasia Basin since the Jurassic (e.g., Shephard et al., 2013).

The Amerasia Basin (Fig. 1a-b) includes the Canada, Makarov, and Podvodnikov basins, the Chukchi Continental Borderland and the Lomonosov, Alpha and Mendeleev ridges. The Canada Basin, which constitutes about a third part of the Amerasia Basin, shows a pseudo-linear magnetic anomaly pattern, which complicates the identification of its nature (e.g., Gaina et al., 2014). According to a recent study, the Canada Basin is composed of extended continental and transitional crust, as well as oceanic crust along a buried extinct mid-ocean ridge (Chian et al., 2016). Continent-ocean boundaries in the Canada Basin displayed in Fig. 1a mostly follow this interpretation. New geophysical data indicate that parts of the Podvodnikov Basin is floored by extended continental crust, at least along the seismic profiles published by Jokat and Ickrath (2015) and Nikishin et al. (2014). The Podvodnikov Basin was interpreted by Alvey et al. (2008) as a Late Cretaceous basin. It has a ca 20 km thick crust, which is derived from gravity inversion and confirmed by refraction data.

Gaina et al. (2014) suggested that the region that flanks the Lomonosov Ridge on the Amerasian Basin side may have accommodated Late Cretaceous-Paleocene extension between the North American and Eurasian plates that preceded the opening of Eurasian Basin. The deep Makarov Basin (~ 4 km) is probably underlain by oceanic crust flanked by stretched continental or transitional crust (Evangelatos and Mosher, 2016; Døssing and Gaina, 2017).

The Chukchi Borderland is a continental fragment (Dietz and Shumway, 1961) that probably rifted from the Canadian Arctic shelf in Jurassic time (Grantz et al., 2011). The origin of the Alpha and Mendeleev Ridges (AMR) is still under debate, since the volcanic overprint perturbs the original tectonic signature and both oceanic and continental crustal natures have been proposed (see for a review Gaina et al., 2014). The Lomonosov Ridge is a continental fragment rifted from the Barents Sea during the Paleocene (e.g., Srivastava, 1985). Extensional phases during Cretaceous and Cenozoic times resulted in the formation of the North Atlantic ocean spreading system (including Baffin Bay), part of the Amerasia basins (the Makarov Basin and possibly part of the Podvodnikov Basin, e.g.,Døssing and Gaina, 2017), and Eurasia Basin, respectively (e.g., Gaina et al., 2014, Nikishin et al., 2018).

The youngest tectonic feature in the Arctic is the active plate boundary between the North American and Eurasian plates resulting from seafloor spreading along the Mohn's, Knipovich, and Gakkel mid-ocean ridges (Fig. 1a-116a). Presently, the Knipovich and Gakkel ridges have an ultra-slow spreading regime (spreading rates $< 20\ mm\ yr^{-1}$, e.g., Dick et al., 2003). Rifting and oceanic crust formation between the North American and Eurasian plates in the Eurasia Basin led to the formation of a large rift system in the Laptev Sea (e.g., Franke et al., 2001). The Baffin Bay (Fig. 1b), with his mid-ocean ridge system, may have been linked with the High Arctic basins from the Paleocene (e.g., Brozena et al., 2003; Døssing et al., 2013), but is now inactive and covered by a thick sedimentary cover.

Large-scale volcanism affected the Arctic region in several episodes. The Siberian Traps were formed on the Siberia craton and also affected parts of Svalbard and East Siberian Islands at the Permian-Triassic boundary (ca. 251 Ma, e.g., Ivanov et al., 2013). One or several volcanic episodes in the Cretaceous affected the High Arctic, most notably the

Alpha and Mendeleev ridges in the Amerasia Basin, but also the Ellesmere Island, the East Siberian Islands, the Franz Josef, and Svalbard archipelagos (Fig. 1a-b) (Maher Jr., 2001; Corfu and Heim, 2013). In the Paleocene, at ca. 61 and 55 Ma, the North Atlantic Igneous province was formed along the NE Atlantic margins (e.g., Storey et al., 2007), and since the Oligocene, volcanic activity affected the NW margin of Svalbard, probably due to the proximity of the mid-ocean ridge (Fig. 1a-b).

3. Data and methods

Below, we describe the approaches and parameters used to obtain self-consistent crustal (sub-Section 3.1), lithospheric thermal (sub-Sections 3.2.1, 3.2.2, and 3.2.3), and strength/*Te* (sub-Section 3.3) models.

3.1. Crustal structure

Global crustal models, such as CRUST 1.0 (Laske et al., 2013) and CRUST 2.0 (Bassin et al., 2000) have been constructed using gravity, seismic, and geological data. They provide first order variations of the crustal parameters, such as thickness, average velocity and density of the main layers. However, due to their coarse resolution (1° × 1° and 2° × 2°, respectively), these models do not fully represent the small scale features. For this study, we used the High Arctic crustal model of Lebedeva-Ivanova et al. (2018) – ArcCRUST -, as it is based on state-of-the-art geophysical data and sediment thickness compilations. This model includes the thickness and density of the crystalline crust and sediments, the boundaries between the continental and oceanic crust, and the age of the oceanic lithosphere, with a resolution of 0.1° x 0.1° (Fig. 2a-d and 3a).

Lebedeva-Ivanova et al. (2018) computed a model for the Moho depth and crystalline crustal thickness of the High Arctic by 3-D gravity forward and inverse modeling in the spectral domain following Minakov et al. (2012) approach and applying a lithosphere thermal gravity anomaly correction as in Alvey et al. (2008). As input for this modeling, the circum-Arctic bathymetric grid (Jakobsson et al., 2012), the gravity anomaly grids (Gaina et al., 2011) and the dynamic topography model of Spasojevic and Gurnis (2012) have been used. An updated sedimentary thickness grid (Fig. 2a) and age distribution of the oceanic lithosphere and a model of the crystalline crust that has variable density are also part of the ArcCRUST model (Fig. 2a-d) and have been used as input data for deriving the crustal thickness. To compute the density of sediments, a relationship between density, depth, and porosity (ϕ) (Athy, 1930) has been taken into account, as shown by eqs. (1) and (2):

$$\rho_s(z) = \rho_{sk}(1 - \varnothing(z)) + \rho_w \varnothing(z) \quad (1)$$

$$\varnothing(z) = \varnothing_0 e^{-Cz} \quad (2)$$

where ϕ_0 is the surface porosity (0.5), C, the compaction coefficient (0.4×10^{-3}), ρ_{sk}, the density of the sedimentary matrix (2650 kg/m^3), and ρ_w, the density of the water (1030 kg/m^3).

In the oceanic realm, the thickness of the crystalline crust in the Eurasia Basin and Greenland Sea ranges between 0.5 and 10 km and thins towards the mid-oceanic ridges (Fig. 2b). It becomes thicker under the Podvodnikov Basin (18–20 km), which is probably partially floored by extended continental crust, the northern Canada Basin (up to ~ 15 km) and the AMR (up to ~ 26 km), due to addition of volcanic material.

The thickness of the continental crystalline crust (*Cr*) varies, depending of the tectonic setting. *Cr* is usually 30–50 km beneath the continents (e.g., Greenland), and thinner, ca. 20–45 km, beneath the continental shelves. The thinnest *Cr* (ca. 15 km) is associated with sedimentary basins in the eastern Barents Sea, the northern part of the Chukchi Sea and the Mackenzie Delta. A similar crustal thickness is observed under the microcontinents in the North Atlantic and a bit thicker (20–35 km) beneath microcontinents in the Arctic Ocean. The southernmost part of the Canada Basin has a crustal thickness of only 4 km in the ArcCRUST model, but is characterized by seismic P-wave velocities of 5.5 to 6.6 km/s and is therefore interpreted as continental crust by Chian et al. (2016).

In this study, *Cr* is divided into an upper (U_C) and lower (L_C) crust of equal thickness. This assumption is roughly consistent with observations from seismic refraction profiles, indicating a proportion between the upper and lower crust in the range of 40–60% (e.g., Pease et al., 2014). The density of the crystalline crust (ρ_c), ranging between 2775 and 2885 kg/m^3 (Fig. 2d) is used to derive the density of the lower crustal layer (ρ_{lc}), assuming that the density of the upper crust (ρ_{uc}) is 2750 kg/m^3, as described in eqs. (3) and (4). This value corresponds to the average density of a mix of granitic, dioritic, and felsic granulite rocks, which are the main components of the upper crust (Christensen and Mooney, 1995). On the other hand, the lower crust has a larger density variability, due to the possible presence of high density magmatic bodies at its bottom.

The only exception is given by the southern Canada Basin, where we assumed a ρ_{uc} equal to 2850 kg/m^3, on account of the anomalous high ρ_c (Fig. 2d), which may indicate the presence of volcanic products and mantle underplating accreted during extension (e.g., Gaina et al., 2014). The resulting ρ_{lc} ranges between 2800 and 2970 kg/m^3, clearly showing a mafic composition.

$$\rho_c = \rho_{uc}(Uc/Cr) + \rho_{lc}\left(1 - \frac{Uc}{Cr}\right) \quad (3)$$

$$\rho_{lc} = \left(\rho_c - \rho_{uc}\left(\frac{Uc}{Cr}\right)\right)\left(1 - \left(\frac{Uc}{Cr}\right)\right)^{-1} \quad (4)$$

These densities are consistent with estimates of Petrov et al. (2016). By analysing seismic, gravity and seismic data, these authors have interpreted that the crustal structure of the Arctic, along the 7600 km long Transpolar Geotransect (crossing the Barents Sea, Franz Joseph Land, Eurasua Basin, Lomonosov Ridge, Podvodnikov Basin, Mendeleev Ridge, Chukchi Sea, and East Siberia) is composed of granulite-gneiss and mafic granulite in its upper and lower crust, respectively.

3.2. Thermal model

The temperature variations throughout the lithosphere are a dominant parameter controlling lithospheric strength (e.g., Burov, 2011). Only in global models, which have used crustal, petrological, and geophysical data as constraints (Artemieva, 2006; Koptev and Ershov, 2011), temperature variations of the Arctic lithosphere have been estimated, assuming steady-state conditions. Below we describe the approaches followed to estimate the continental and oceanic thermal field.

3.2.1. Steady-state approach

Continental crust may have undergone various thermal events throughout its history and a major part of the surface heat flow (*HF*) is controlled by the high variance of the radiogenic heat generation (*HG*) within the continental crust (Burov, 2011). The *HG*, caused by the decay of the elements uranium, thorium and potassium, is responsible for 20–40% of the heat loss through the continental domains (Artemieva and Mooney, 2001; Hasterok and Chapman, 2011; Pollack and Chapman, 1977). Assuming steady-state conditions and neglecting the transient effects of erosion, deposition of sediments, and processes of advection, the temperatures and heat flow vary with depth, according to eq. (5) and (6).

$$T_{i+1} = T_i + \frac{q_i}{k}\Delta z - \frac{HG_i}{2k}\Delta z^2 \quad (5)$$

$$q_{i+1} = q_i - HG_i \Delta z \quad (6)$$

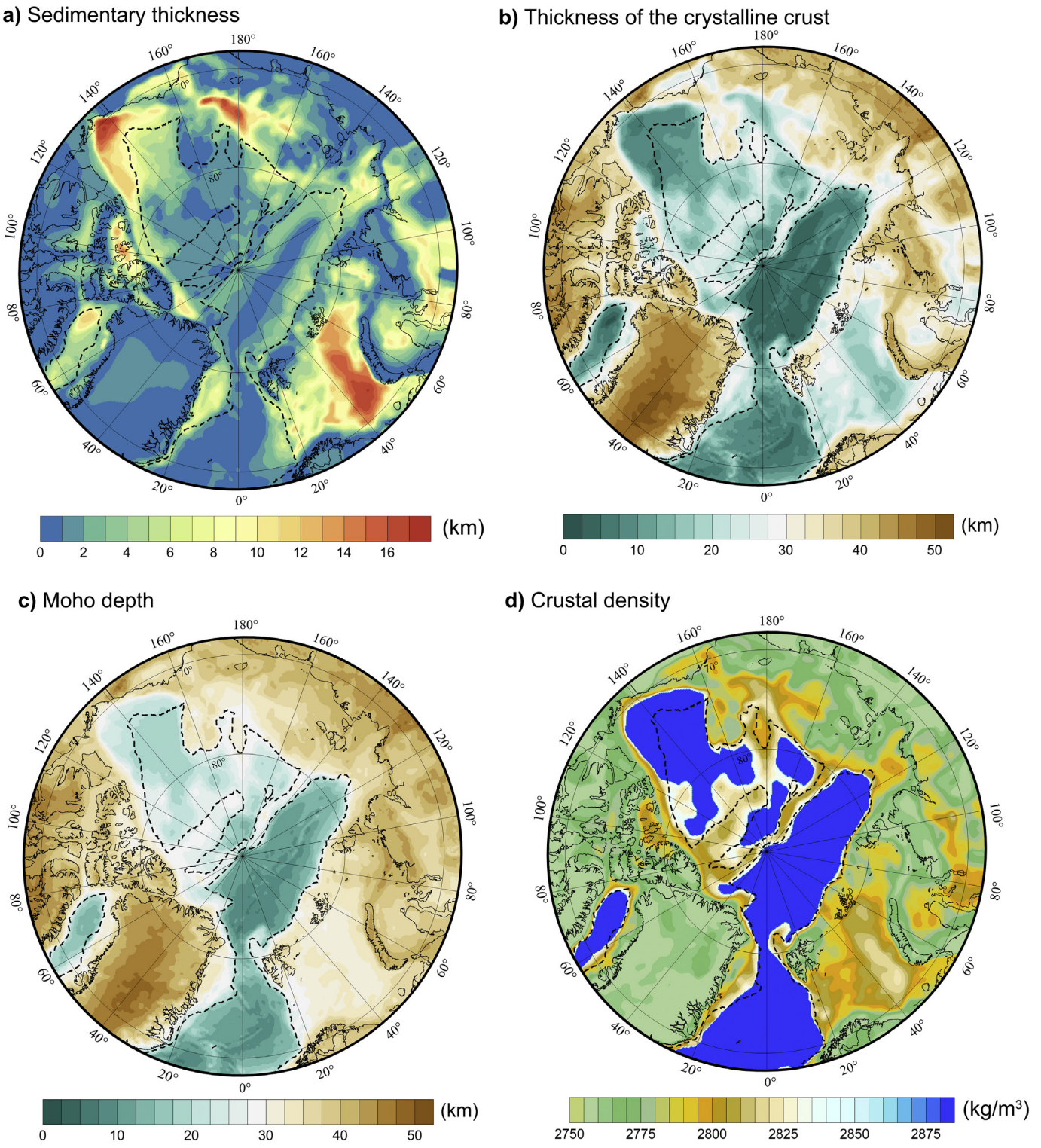

Fig. 2. Lithospheric model of Lebedeva-Ivanova et al. (2018). (a) Sedimentary thickness; (b) thickness of the crystalline crust (c) Moho depth; (d) crustal density.

Following the approach of Chapman (1986), the temperature (T_{i+1}) and heat flow (q_{i+1}) at the bottom of each layer are estimated based on the T_i and q_i at the top of each layer with a Δz of 0.5 km, where the surface temperature is 0 °C. The HG_i and k_i are the radiogenic heat generation and the thermal conductivity for each layer i, respectively. The surface *HF* (q_0) data are unevenly distributed in the study area and, in particular, the ice covered areas of Greenland and Canadian Arctic are almost unsampled. In order to identify the surface heat flow values which may represent the thermal conditions of the Arctic lithosphere, we analysed the Global Heat Flow Database of the International Heat Flow Commission (IHFC) (http://www.heatfow.und.edu/) and the global model of surface heat flow of Davies (2013), displayed in Fig. 3b. The first dataset provides surface *HF* data mainly located in the Greenland Sea, Barents Sea, and the shelves of the Canadian Arctic. The global model of Davies (2013), which has a uniform resolution of 2° × 2°, presents heat flow estimates based on the correlation between 38,374 existing measurements and different geologic domains, defined by global digital geology maps. The distribution of the surface *HF*

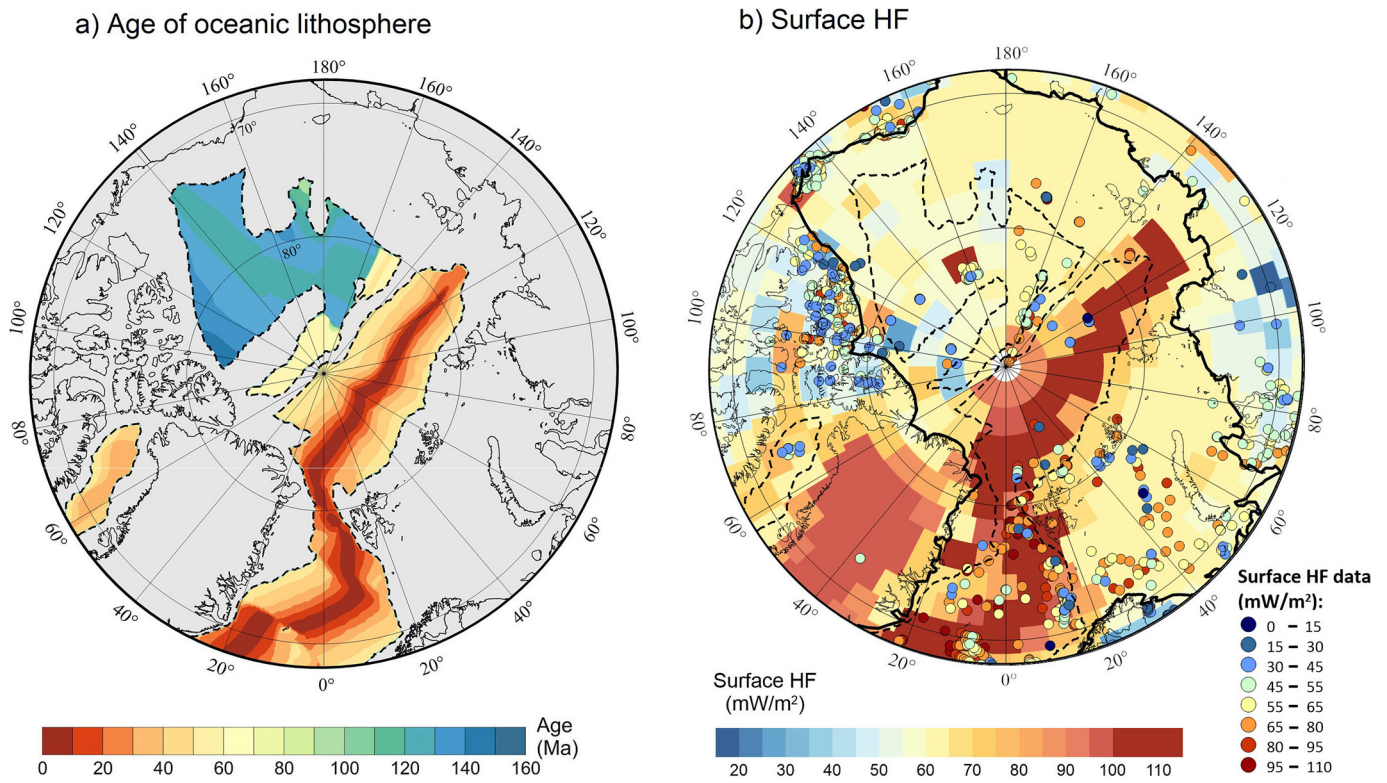

Fig. 3. (a) Age of the oceanic lithosphere. (b) Map of modeled surface *HF* from Davies (2013). The colored dots indicate the *HF* measurements available from the IHFC database (http://www.heatfow.und.edu/). The thick black line illustrates the division between continental mainland, with estimated surface *HF* of 50 mWm^{-2} and continental shelf, with estimated surface *HF* of 62 mWm^{-2}. (For interpretation of the references to colour in this figure legend, the reader is referred to the web version of this article.)

values in both datasets shows that the offshore and onshore continental domain are characterized by respectively elevated (> 55 mWm^{-2}) and reduced (< 55 mWm^{-2}) estimates (Fig. 3b). In particular, Davies (2013) estimated for most of the continental offshore areas a value of 62 mWm^{-2}, while in the onshore regions the surface heat flow mainly ranges between 25 mWm^{-2} and 60 mWm^{-2}. For this reason, we divided the continental part of the study area in onshore and offshore domains, assigning to them a surface *HF* of 50 mWm^{-2} and 62 mWm^{-2}, respectively. This assumption is in overall agreement with the most recent estimates of surface *HF*, indicating in the East Siberian continental slope and southern Lomonosov Ridge an average value of 57 mWm^{-2} (O'Regan et al., 2016). It should be noted that Greenland, which lacks measurements of surface *HF* data, is the largest continental area of the Arctic, where our heat flow boundary condition cannot be validated. The global map of Davies (2013) predicts in this region an anomalous high surface *HF* (95 mWm^{-2}), while according to the recent model of Rogozhina et al. (2016), the heat flux at a depth of 5 km from the surface topography is only anomalously high (75–106 mWm^{-2}) in the central-eastern part of Greenland. However, we prefer to assign the same value used for the other onshore areas (50 mWm^{-2}), since it is more consistent with values characterizing tectonic features of Archean-Proterozoic age (e.g., Jaupart and Mareschal, 1999). The values of *HG* and *k* of the crust and mantle lithosphere are displayed in Table 1. Below we describe the assumptions and approaches used to derive them.

We estimated the *HG* in the upper crust (HG_{uc}) using the partition model of Hasterok and Chapman (2011). In this model HG_{uc} is expressed by:

$$HG_{uc} = \frac{xq_s}{D_{uc}} \tag{7}$$

According to this model, a fraction (x) of the surface *HF* (q_s) results from the upper crustal radiogenic heat sources, where D_{uc} is the thickness of the upper crust. The remaining fraction (1-x) comes from other sources, where the sediments, lower crust, lithospheric and sublithospheric mantle contributes to the residual *HF*.

The fraction x has been assumed in previous studies to be equal to 0.4 (Chapman, 1986), 0.26 (Hasterok and Chapman, 2011), and 0.33–0.29 (Artemieva and Mooney, 2001), according to different values and models of thermal conductivity and heat production distributions. In this study, we adopted the value of 0.26, which has been estimated by Hasterok and Chapman (2011) on the base of petrologic data and thermal conductivity results obtained from several recent laboratory studies. The resulting geotherms (Fig. 4a), estimated using the partition model of Hasterok and Chapman (2011) and Artemieva and Mooney (2001), are very similar. In contrast, the temperatures, estimated

Table 1
Thermal parameters for the continental lithosphere. See text for further explanation.

Parameter	Symbol	Units	Sediments	Upper crust	Lower crust	Upper mantle
Composition				Granite	Mafic granulite	Olivine
Heat Generation	*H*	μWm^{-3}	1.18	0.5–4.5	0.5	0.02
Thermal Conductivity	*k*	mWm^{-2}	1.2–2.5	3.0	2.6	variable

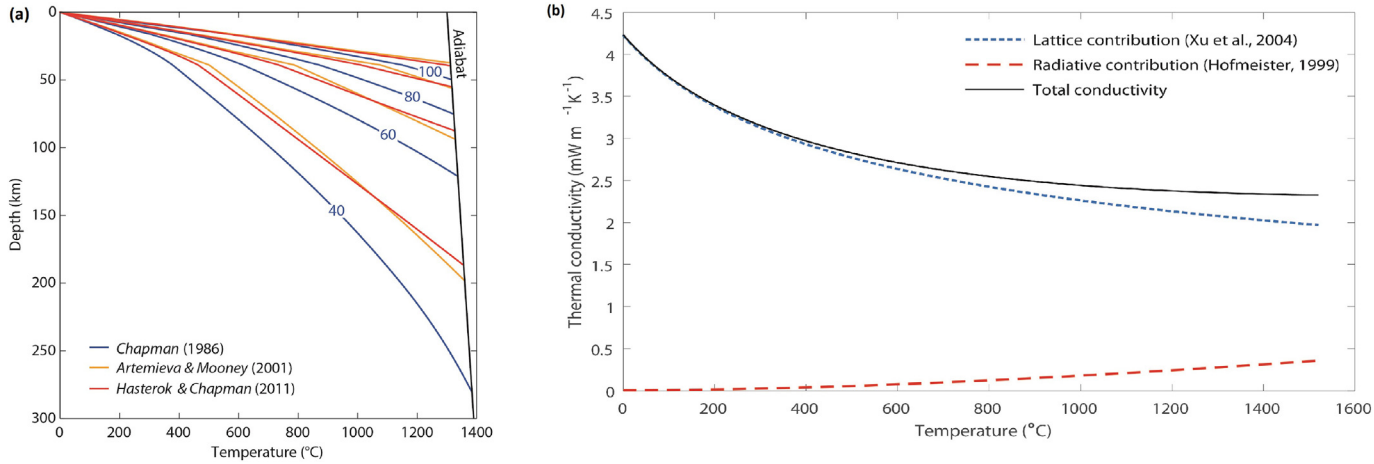

Fig. 4. (a) Steady-state geotherms for different surface heat flows (40, 60, 80 and 100 mWm^{-2}), computed for a Moho depth of 39 km, based on the study of Chapman (1986) (in blue), Artemieva and Mooney (2001) (in yellow), and Hasterok and Chapman (2011) (in red). (b) Temperature dependence of the conductivity of the lithospheric mantle. The dotted and continuous blue lines show the lattice (Xu et al., 2004) and radiative (Hoffmeister, 1999) component of the conductivity, respectively. The sum of the two effects is represented by the solid black line.

adopting the model of Chapman (1986), are significantly lower in the mantle lithosphere (~200 °C at a depth of 100 km).

The *HG* of the sediments, which can span a large range (0.32 to 1.80 μWm^{-3}, Vilà et al., 2010) is assumed to be equal to 1.18 μWm^{-3}, which is an average value for detritic sediments (Vilà et al., 2010) and for the sediments deposited in the Kara and Barents Sea (Klitzke et al., 2016). According to Eq. (7), an increase of the thickness of the upper crust results in a decrease of its *HG* and vice versa. Therefore, HG_{uc} reaches a minimum value of 0.5 μWm^{-3} for a q_s of 50 mWm^{-2} and a maximum D_{uc} (25.5 km). On the other hand, for very thin D_{uc} (< 3.7 and 2.8 km, for a q_s of 50 mWm^{-2} and 62 mWm^{-2}, respectively), occurring in some parts of the Canada basin, HG_{uc} increases over 4.5 μWm^{-3}. Since HG_{uc} rarely reaches values of 4.8 μWm^{-3} (Hasterok and Chapman, 2011), we limited its value to 4.5 μWm^{-3}. We made this choice also considering that the steady state approach is likely not applicable in this part of the Canada basin, being characterized by a very thinned crust.

We assigned to the lower crust a *HG* equal to 0.5 μWm^{-3}, which is a representative value for lithologies, such as mafic granulite (0.15–0.5 μWm^{-3}) and diorite (0.47–1.21 μWm^{-3}), which usually compose this layer (Rybach and Buntebarth, 1982; Vilà et al., 2010). The mantle lithosphere has a *HG* much lower than the crust, and thus a value of 0.02 μWm^{-3} is adopted (Hasterok and Chapman, 2011).

The thermal conductivity (k) varies over a wide range for different rocks types, even for the same rock, depending on variations in composition, anisotropy, and degree of compaction (e.g., Hantschel and Kauerauf, 2009). For *k* of the sediments (k_s), compaction was accounted for by using the geometric mean model, described by:

$$k_s = k_b^{1-\varnothing_z} k_w^{\varnothing_z} \tag{8}$$

where we assumed that the bulk thermal conductivity, k_b, is equal to an average value for the sediments deposited in the Kara and Barents Sea (2.46 $Wm^{-1}K^{-1}$, Klitzke et al., 2016) and the conductivity of water, k_w, is equal to 0.6 $Wm^{-1}K^{-1}$. The variation of porosity with depth (ϕ_z) is estimated from eq. (2). The resulting k_s from the surface up to a depth of 18 km ranges within 1.2 - 2.5 $Wm^{-1}K^{-1}$. Rocks that more likely compose the upper crust, such as quartzite and granite, have a *k* varying within 1.2 - 4.5 $Wm^{-1}K^{-1}$ and 3–7.9 $Wm^{-1}K^{-1}$, respectively. In contrast, *k* of rocks that usually are the main components of the lower crust, such as diorite and mafic granulite, is significantly lower, ranging within 1.8 - 4.1 $Wm^{-1}K^{-1}$ and 2.5–3 $Wm^{-1}K^{-1}$, respectively (Zoth and Haenel, 1988; Seipold, 1992). Based on these wide ranges of estimates, we used an average value of *k* for the upper and lower crust, equal to 3 $Wm^{-1}K^{-1}$ and 2.6 $Wm^{-1}K^{-1}$, respectively. We estimated *k* of the lithospheric mantle, as temperature dependent, taking into account both the lattice (Xu et al., 2004) and radiative (Hoffmeister, 1999) component (Fig. 4b). The sum of the two components results in a decrease of *k* from 3.0 $Wm^{-1}K^{-1}$ to 2.3 $Wm^{-1}K^{-1}$ in the temperature range of 400–1350 °C (Fig. 4b).

3.2.2. Plate model

We adopt the plate model commonly used to describe oceanic lithospheric cooling (McKenzie, 1967). According to this model, the temperature field is in equilibrium and the ridge parallel horizontal heat conduction is negligible and thus not considered. We used the GDH1 (Global Depth Heat) plate model of Stein and Stein (1992), since this model gives the best-fit with global heat flow data and with the bathymetry of old oceanic lithosphere (> 70 Ma), compared to the previous plate cooling model of Parsons and Sclater (1977). The thermal boundary conditions used in the GDH1 plate model are the following: (a) a fixed basal temperature at the bottom of the plate ($T = T_m$ at $z = L$); (b) a constant temperature at the initial state of the plate ($T = T_m$ at $t = 0$, where t is the age of the lithosphere); (c) a constant temperature of 0 °C at the surface of the ocean ($T = 0$ °C at $z = 0$). Therefore, temperatures are estimated according to Eq. (9), with a step along the vertical direction z of 0.5 km:

$$T(z) = T_m \left[\frac{z}{L} + \sum_{n=1}^{\infty} \frac{2}{n\pi}(-1)^{n+1} exp\left(-\frac{n^2\pi^2\kappa}{L^2}t\right) sin\left(\frac{n\pi z}{L}\right) \right] \tag{9}$$

where L (95 km) is the asymptotic thermal plate thickness and κ is the thermal diffusivity (0.804×10^{-6} $m^2 s^{-1}$), which controls the flow of heat by conduction and depends on C_p, the heat capacity at constant pressure, and ρ, the density.

In the calculation, the age of the oceanic lithosphere is taken from the study of Lebedeva-Ivanova et al. (2018). As the thickest (> 3 km) part of the sediment cover is situated on top of relatively old (> 50 Ma), thus strong oceanic lithosphere, the sediments are considered as part of the oceanic plate, as they will hardly affect the plate's thermo-mechanical characteristics. Transient thermal effects induced by mantle uprising along the spreading ridge will affect the oceanic plate only locally.

To prevent a sharp thermal transition between the oceanic and continental domain and the onshore and offshore continental regions, characterized by two different surface *HF* values, we incorporated a 100 km wide transition zone in which temperatures were interpolated by kriging.

3.2.3. Thermal model from inversion of seismic tomography

In order to compare the results of the new thermal model with temperatures obtained from independent data, we inverted seismic velocities of the upper mantle of the Circum-Arctic into temperatures. For this purpose, we chose the regional tomography model of Yakovlev et al. (2012), with seismic anomalies showing a clear correlation with the main lithosphere structures in the Circum-Arctic region. Other regional models cover only a part of the study area (e.g., Rickers et al., 2013), while the global models do not have a comparable resolution (e.g., Ritsema et al., 2011; Schaeffer and Lebedev, 2013).

The seismic tomography model of Yakovlev et al. (2012) is based on travel times of body *P*-waves from the worldwide catalog of the International Seismological Center (ISC) for the time period from 1964 to 2007. The travel times have been corrected for the Earth ellipticity, elevations of stations, and the crustal thickness based on the global CRUST2.0 model (Bassin et al., 2000). The tomographic inversion was performed based on an approach developed by Koulakov et al. (2002), using as a velocity reference the 1D spherical model AK135 (Kennett et al., 1995).

The inversion of seismic velocity into temperatures (see for details, Appendix 1 in Kaban et al., 2014) is computed by (1) estimation of the synthetic anharmonic velocities of the main mantle phases (olivine, OPX, CPX, and garnet) at elevated pressures and temperatures, using the mineral physics approach of Stixrude and Lithgow-Bertelloni (2005); (2) correction of the anharmonic velocities for anelasticity effect; (3) comparison of the resulting synthetic velocities with those of the seismic tomography model. In the inversion, we assumed a uniform "fertile" composition, which is defined in this study as an average of the mineral fractions constituting the "Primitive mantle" rock (McDonough and Sun, 1995) and the "Tecton garnet peridotite" rock (Griffin et al., 2003). We used the attenuation model *Q4* of Cammarano et al. (2003), which is more representative of the generally "hydrated" conditions of a "fertile" upper mantle (Tesauro et al., 2014). Since the upper mantle of the cratonic areas is usually in 'dry' conditions, the temperatures in this regions may be underestimated by ~100 °C (Cammarano et al., 2003), at temperatures > 900 °C, when the anelasticity is activated (Jackson et al., 2002).

As discussed in previous studies (e.g., Tesauro et al., 2012), the inversion of seismic velocities into temperatures is also affected by uncertainties (± 100–150 °C), which are mainly inherited from the seismic tomography models. These usually do not provide direct estimations of the velocity uncertainties, which depend on numerous factors, including the applied crustal correction, reference seismic model used, and inhomogeneous ray coverage (see for a review Foulger et al., 2013). Other uncertainties related to the inversion depend on the compositional and anelasticity model used. The assumption of a "fertile" upper mantle may not be suitable for the cratonic areas (e.g., Greenland), as it may be affected by depletion of heavy constituents (e.g., garnet). However, these uncertainties are likely small (< 100 °C), considering that *P*-waves are much less sensitive to compositional variations than *S*-waves (e.g., Goes et al., 2000).

3.3. Lithospheric strength and effective elastic thickness (Te)

The bulk strength of the lithosphere, which predicts the maximum differential stress required for rocks failure (Ranalli, 1994), is commonly described by the yield strength envelope (*YSE*, Goetze and Evans, 1979). The YSE (Fig. 5) allows quantitative assessment of lithospheric strength based on experimentally determined constitutive equations, describing brittle and ductile behavior of rocks (e.g., Brace and Kohlstedt, 1980). The integrated strength has been estimated on a global and regional scale in previous studies, by integrating the YSE with respect to depth (Tesauro et al., 2009, 2013, and 2015). The first-order results of these previous studies are in overall agreement with inferences obtained from inverse approaches based on coherence analysis (Tesauro et al., 2012). The brittle strength is described by Byerlee's

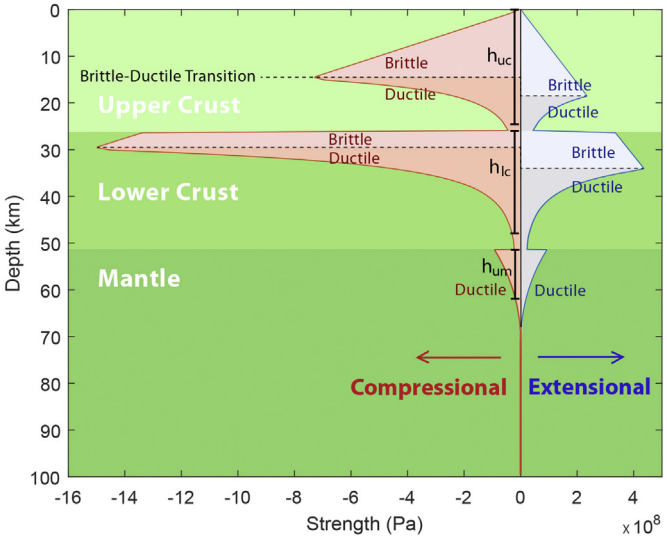

Fig. 5. Example of Yield Strength Envelope (YSE) for continental lithosphere, estimated for compressional (red) and extensional (blue) conditions. (For interpretation of the references to colour in this figure legend, the reader is referred to the web version of this article.)

law (Byerlee, 1978):

$$\sigma = \alpha \rho g z (1 - \lambda) \tag{10}$$

where α is the friction coefficient, ρ the density, g the gravity constant, λ the pore fluid factor and z the depth of the bottom of the layer (Table 2). For extensional regimes like the Arctic, the friction coefficient is equivalent to 0.75 (e.g., Afonso and Ranalli, 2004).

In ductile conditions crustal rocks deform according to power-law dislocation creep at high stresses and moderate temperature (< 1300 °C):

$$\sigma = \left[\frac{\dot{\varepsilon}}{A_P}\right]^{\frac{1}{n}} \cdot \exp\left[\frac{E_P}{nRT}\right] \tag{11}$$

where $\dot{\varepsilon}$ is the strain rate, A_p the power-law strain rate, n the power-law exponent, E_p the power-law activation energy, R the Gas constant and T the temperature (Table 2).

In the uppermost mantle at high stress and relatively low temperatures (< 1000 °C), the ductile deformation occurs more likely according to the creep mechanism, known as 'low-temperature plasticity' or 'Dorn law' (e.g., Ranalli and Adam, 2013). We used the results of the most recent laboratory experiments deriving the exponential flow law applicable to the uppermost mantle (Demouchy et al., 2013):

$$\sigma = \sigma_D \left\{1 - \left[-\frac{RT}{E_D} \ln\left(\frac{\varepsilon}{A_D}\right)\right]^{1/2}\right\}^2 \tag{12}$$

where σ_D is the Dorn law stress, E_D the Dorn law activation energy and A_D the Dorn law strain rate (Table 2). This new semi-empirical exponential flow law, based on experiments on single olivine crystals in the range of temperature of (800–1090 °C) and at a confining pressure of 300 MPa, has demonstrated that the strength of lithospheric mantle

Table 2
Thermal parameters for the oceanic lithosphere. See text for further explanation.

Parameter	Symbol	Units	GDH1
Surface temperature	T_0	^{0}C	0
Basal temperature	T_m	^{0}C	1350
Asymptotic plate thickness	L	km	95
Thermal diffusivity	κ	$m^2 s^{-1}$	0.804×10^{-6}

has been significantly overestimated using previous flow laws (e.g., Evans and Goetze, 1979; Mei et al., 2010). On account of the mafic composition of the Arctic crust, we assigned a "dry granite" and "mafic granulite" rheology to the upper and lower crustal layer, respectively. A "dry" olivine rheology is assumed for the mantle lithosphere for both continental and oceanic domains, since the creep parameters are not defined for a "wet" rheology. The last one is likely more representative of the conditions of continental mantle lithosphere recently involved in subduction of oceanic lithosphere and post-Paleozoic tectonothermal events, such as characteristic for the old oceanic South Anyui Basin. Therefore, in this area the estimated strength is an upper bound of the possible values depending on the degree of hydration of the upper mantle. We used a uniform value of strain rate equal to $1 \times 10^{-15}\,s^{-1}$, which is commonly observed in tectonically relatively stable areas (e.g., Kreemer et al., 2014). However, we should take into account that the strain rate may vary of about two orders of magnitude in areas characterized by fast or slow deformation (e.g., Kreemer et al., 2014). The effect on strength of variations of one order in the strain rate is discussed in Tesauro et al. (2015). The integrated strength is calculated for both compressional and extensional stress, but only results obtained for extensional conditions are discussed in Section 3.2.1. Indeed, as before discussed, most of the Arctic regions are rifted continental margins and thus have primarily experienced extensional tectonics. For compressional conditions the coupling/decoupling conditions and the effective elastic thickness remain unchanged (Fig. S1). The rheological parameters and strength equations for both the crust and upper mantle are displayed in Table 3.

From the computed YSE it is possible to define the thickness of the mechanically strong part of the lithospheric layers that extends from the top of the layer to the depth associated to a specific geotherm (e.g., 350 °C for quartzite), at which the yield stress is less than some predefined value (e.g., 10 MPa used in Ranalli, 1994). The lithospheric layers are considered decoupled when the strength decreases below this threshold; otherwise the layers are considered coupled. *Te* is calculated as the sum of the mechanically strong layer thicknesses (Δh_i), depending on the coupled and decoupled behaviour of the layers (Burov and Diament, 1995), as described by eqs. (13) and (14).

$$\text{coupled layers: } T_e^{(n)} = \left(\sum_{i=1}^{n} \Delta h_i\right) \tag{13}$$

$$\text{decoupled layers: } T_e^{(n)} = \left(\sum_{i=1}^{n} \Delta h_i{}^3\right)^{1/3} \tag{14}$$

4. Results and discussion

4.1. Thermal model

The thermal model obtained in this study (named ThermoSteadyState model) is displayed in terms of temperature distributions at a depth of 40 km and 100 km (Fig. 6a-b) and along three cross-sections: A-A′, crossing Greenland, the Lomonosov Ridge, and the New Siberian islands; B-B′ crossing the Barents Sea, the Eurasia Basin, and the Amerasia Basin; and C-C′ crossing the Kara Sea, the Eurasia Basin, and the Ellesmere islands (Fig. 7). Furthermore, the heat flow at the Moho depth and at the bottom of the lithosphere, estimated as the depth of the isotherm 1350 °C, are shown in Figs. 8(a-b).

At the depth of 40 km the continental lithosphere has the lowest temperatures (~450 °C) in the Sverdrup and Yenisey Khatanga Basin, where the surface *HF* is assumed 50 mWm^{-2} and the depth of the Moho is reached at relatively shallow depth for the continental mainland (30–35 km). In contrast, the highest temperatures (~ 700 °C) are observed in the east continental shelves (Chukchi Borderland, East Siberian Sea, New Siberian islands, and North Kara Basin), where the surface *HF* is assumed to be 62 mWm^{-2}, and the depth of the Moho is reached at relatively larger depths for the continental shelf (> 40 km). A similar thermal variation is also observed at a depth of 100 km, where the temperatures in the eastern continental shelves already reach 1350 °C, while the Sverdrup and Yenisey Khatanga basin shows temperatures of ~ 850 °C. Indeed, different conditions in terms of crustal structure and surface heat flow between these continental regions result in a low (< 20 mWm^{-2}) and high (62 mWm^{-2}) Moho *HF* (Fig. 8a), which consequently lowers and increases the temperatures in their mantle lithosphere, respectively. The Sverdrup Basin and Yenisey Khatanga Basin are also characterized by a relatively thick lithosphere (150–180 km) with respect to the eastern continental shelves

Table 3
Rheological parameters. Numbers indicate the following: [1] Carter and Tsenn (1987); [2] Wilks and Carter (1990); [3] Demouchy et al. (2013). See text for further explanation.

Parameter	Symbol	Units	Sediments	Upper crust	Lower crust	Oceanic crust	Upper mantle
Composition				Granite (dry) [1]	Mafic granulite [2]	Diabase [1] (dry)	Olivine [3]
Brittle strength							
Brittle Law	$\sigma_b = f\,\rho g z(1-\lambda)$						
Friction coefficient	α	0.75	0.75	0.75	0.75		0.75
Density	$\rho\ \sigma$	$kg\,m^{-3}$	1825–2650	2750–2850	2760–3020	2776–2885	3330
Thickness	D	km	0–18	2–25.5	1–15	0–33	
Gravity constant	g	$m\,s^{-2}$	9.81	9.81	9.81	9.81	9.81
Pore fluid factor	λ	–	0.36	0.36	0.36	0.36	0.36
Ductile strength							
Power law	$\sigma = \frac{\dot{\varepsilon}}{A_p}^{\frac{1}{n}} \exp\left[\frac{E_p}{nRT}\right]$						
Dorn law	$\sigma = \sigma_D\left(1 - \left[-\frac{RT}{E_D}\ln\left(\frac{\dot{\varepsilon}}{A_D}\right)\right]^{\frac{1}{2}}\right)^2$						
Strain rate	$\dot{\varepsilon}$	s^{-1}	10^{-15}	10^{-15}	10^{-15}	10^{-15}	10^{-15}
Power law strain rate	A_p	$Pa^{-n}s^{-1}$		3.16×10^{-26}	8.83×10^{-22}	6.31×10^{-20}	7.0×10^{-14}
Power law exponent	n	–		3.3	4.2	3.05	3
Power law activation energy	E_p	$kJ\,mol^{-1}$		186.5	445	276	510
Gas constant	R	$J\,K^{-1}\,mol^{-1}$	8.31	8.31	8.31	8.31	8.31
Dorn law stress	σ_D	Pa					15×10^9
Dorn law activation energy	E_D	$kJ\,mol^{-1}$					450
Dorn law strain rate	A_D	s^{-1}					1.0×10^6

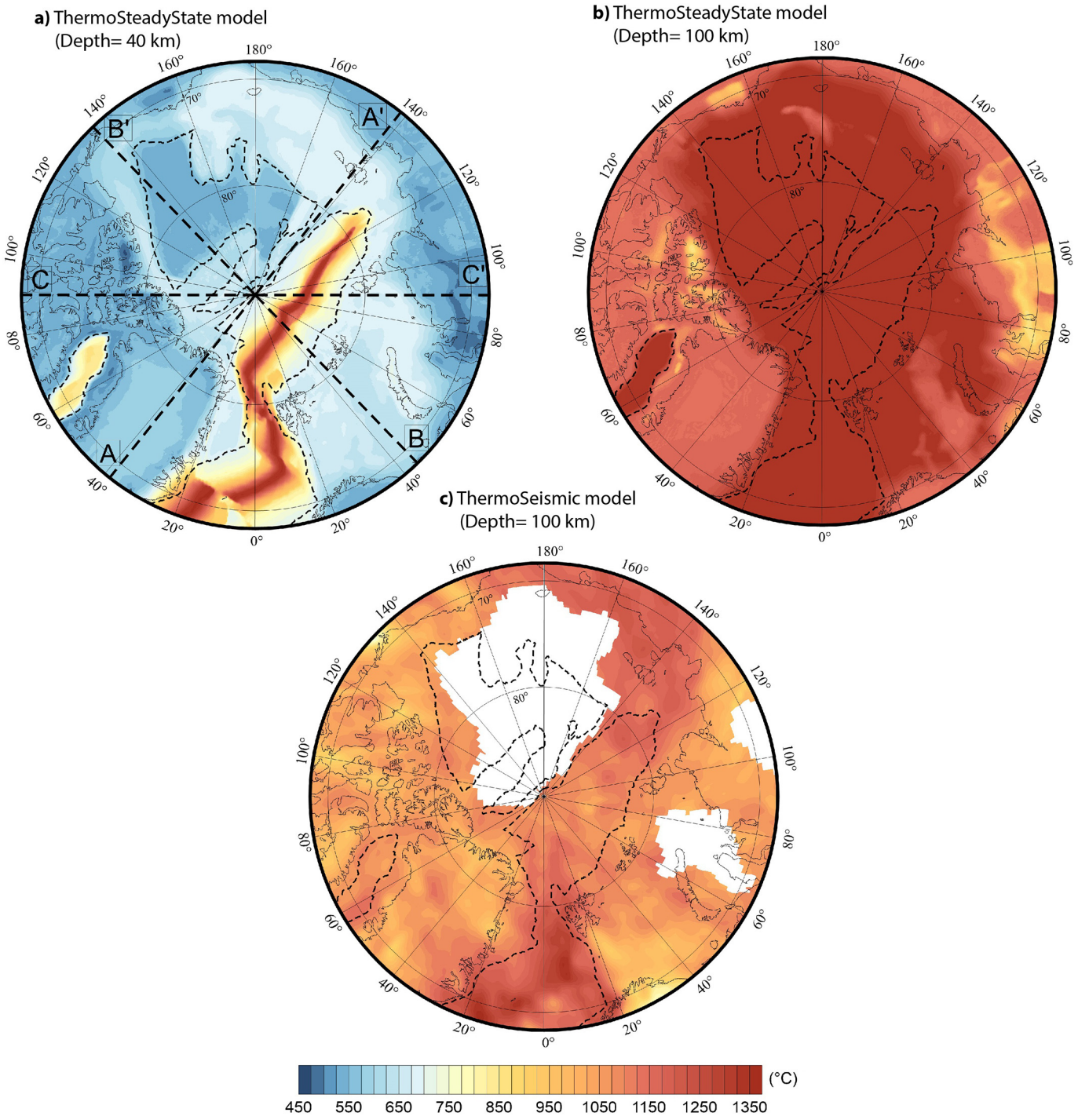

Fig. 6. Final temperature models estimated using steady-state conditions and plate model in the continental and oceanic area, respectively, at a depth of (a) 40 km and (b) 100 km (ThermoSteadyState model) and (c) obtained from the inversion of the regional seismic tomography model of Yakovlev et al. (2012) at a depth of 100 km depth (ThermoSeismic model). Thick black dashed lines in Fig. 6a indicate the location of the three cross-sections displayed in Figs. 7 and 10.

(85–115 km) (Fig. 8b). The depth of the lithosphere, as estimated in the study of Klitzke et al. (2015) based on surface wave tomography models of Levshin et al. (2007) and Shapiro and Ritzwoller (2002), deepens from 120 km in the Barents Sea to 160 km in the Kara Sea. This deepening is not observed in our model, since the Barents Sea is underlain by a thinner crust and thick sediment cover, which lowers the temperature in the mantle and increases the thickness of the LAB with respect to the Kara Sea, characterized by a thicker crust and low sediment cover (Fig. 1a and 1b).

The temperatures at a depth of 100 km, estimated from inversion of seismic tomography data (named ThermoSeismic model), are in general up to 200 °C lower than those of the ThermoSteadyState model (Fig. 6c). Such a difference is within the range of uncertainties affecting the assumptions used in both the seismic inversion and steady-state approach. At the same time, we can observe that the temperature variation observed between the relatively cold Sverdrup and Yenisey Khatanga Basin and warm east continental shelves is also identified in the ThermoSeismic model, indicating that these results are comparable. Most of the Arctic shelf area was affected by rifting during the Mid-Late Cretaceous and Paleocene, a period that preceded seafloor spreading in

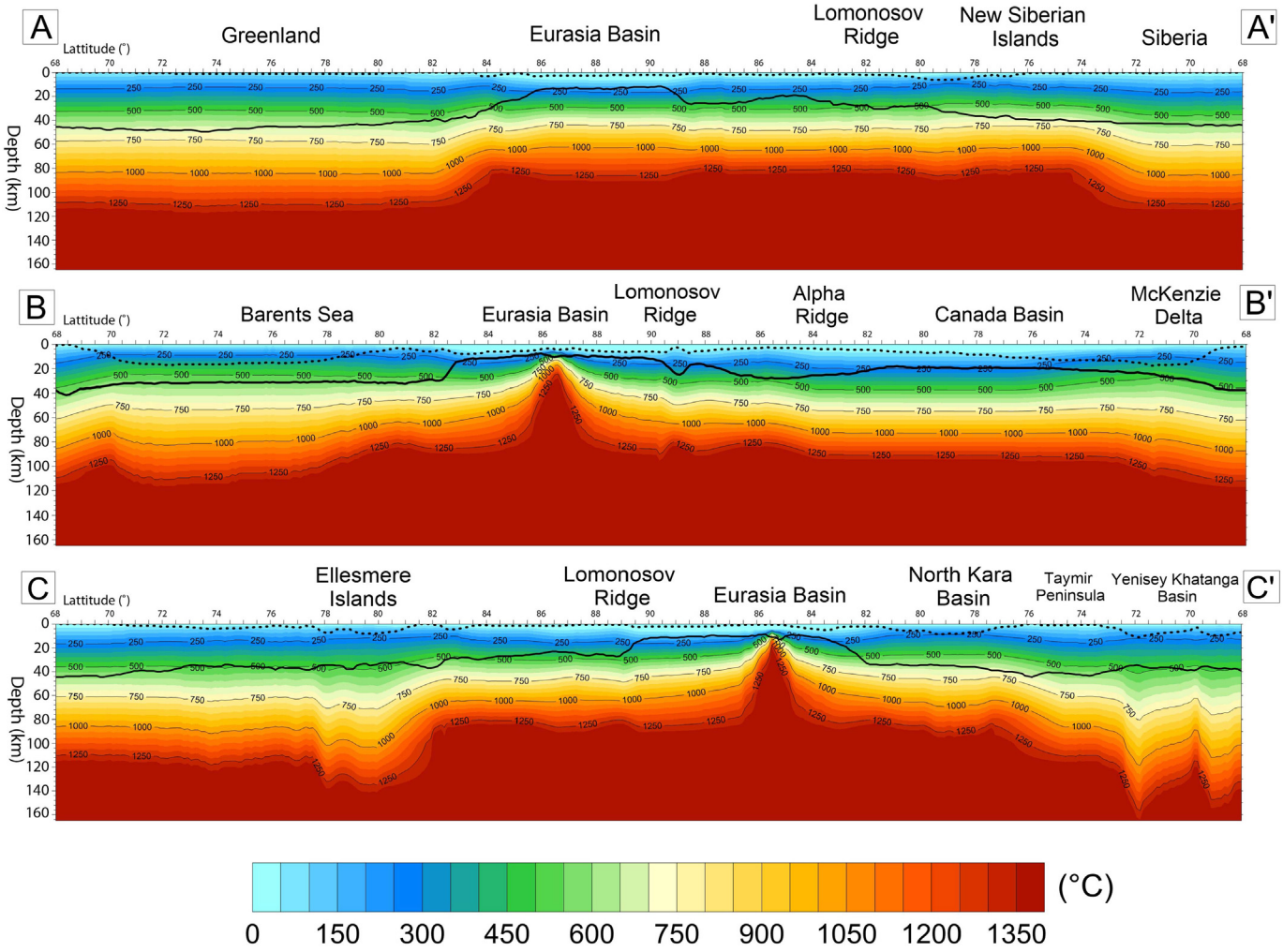

Fig. 7. Temperature distribution along three cross-sections, displayed in Fig. 6a. Latitudes and depths are displayed along the *x*-axis and *y*-axis, respectively. The continuous and dashed black lines show the depth of the Moho and basement, respectively.

the Amerasia and Eurasia basins and Northernmost North Atlantic, respectively. In particular, the NW Svalbard, East Siberian Shelf, and Chuchki region experienced crustal thinning and vertical motions (e.g., Dörr et al., 2012) which may explain the higher temperatures shown by our models.

In the onshore continental lithosphere, temperatures are low (< 600 °C at a depth of 40 km) in areas which have been stable over geological time, such as Greenland, the Canadian Arctic, Siberian and Baltic cratons (Fig. 1). In these regions, the steady-state approach is more suitable than in tectonically active areas, as suggested by the overall consistency with the results of the ThermoSeismic model. Notably, in Greenland the temperatures at 40 km depth increase from the margins to the center, according to the increase of crustal thickness (Lebedeva-Ivanova et al., 2018). In contrast, at a depth of 100 km the temperatures are slightly lower in western central Greenland than in other parts of this region (Fig. 6a and b), since the sedimentary cover of 4–5 km (Fig. 1a) lowers the Moho *HF* (Fig. 8a). Unfortunately, there are no xenolith data in the inner part of Greenland, which can further constrain these results. On the other hand, the ThermoSeismic model shows that high thermal anomaly regions at a depth of 100 km are crossing Greenland from E to NW, coinciding with location of higher melt rates of ice (e.g., Fahnestock et al., 2001). This feature is not observed in the ThermoSteadyState model, since we assumed in this region a uniform surface heat flow value (50 mWm^{-2}). We estimated a thickness of the lithosphere in Greenland between 120 and 125 km, which is less than the values estimated in the cratonic areas (e.g., Yuan and Romanowicz, 2010) and by the seismic tomography model of Yakovlev et al. (2012). At the same time, the S-velocity model of Rickers et al. (2013) predicts a large lithospheric thickness (160–200 km) only in northern and southwestern Greenland and a significant reduction (< 100 km) towards the eastern part. Kumar et al. (2005), using the *S*-receiver functions technique, estimated a thinning of the lithosphere from 120 km along the western margin to 70–80 km in the center and along the eastern margin of Greenland, probably related to the traceable track of the Iceland plume. More recently, Rogozhina et al. (2016) hypothesized that thin lithosphere is present in the central and eastern Greenland. Few xenolith data collected along the eastern and western margins of Greenland predict lithospheric temperatures above typical values for an Archean cratonic geotherm (Bernstein et al., 1998, 2006). Therefore, the lithospheric thickness of Greenland is likely more heterogeneous than shown by our estimates, which can be considered representative of an average value for this tectonic block.

In the oceanic domain, where we estimated temperatures according to the plate cooling model (Section 3), at a depth of 40 km the largest values (900–1350 °C) are observed close to the spreading ridges in the Eurasia Basin and Greenland Sea (Fig. 6a) and are linked to the process of active spreading. Temperatures decrease away from the spreading ridge, as observed in the Eurasia Basin (Section B-B′, Fig. 7), and reach minimum values of 530 °C in the old Amerasia Basin. Consequently, the depth of the lithosphere ranges from a few kilometers beneath the ridge to ~ 90 km beneath the oceanic-continental boundary and Amerasia

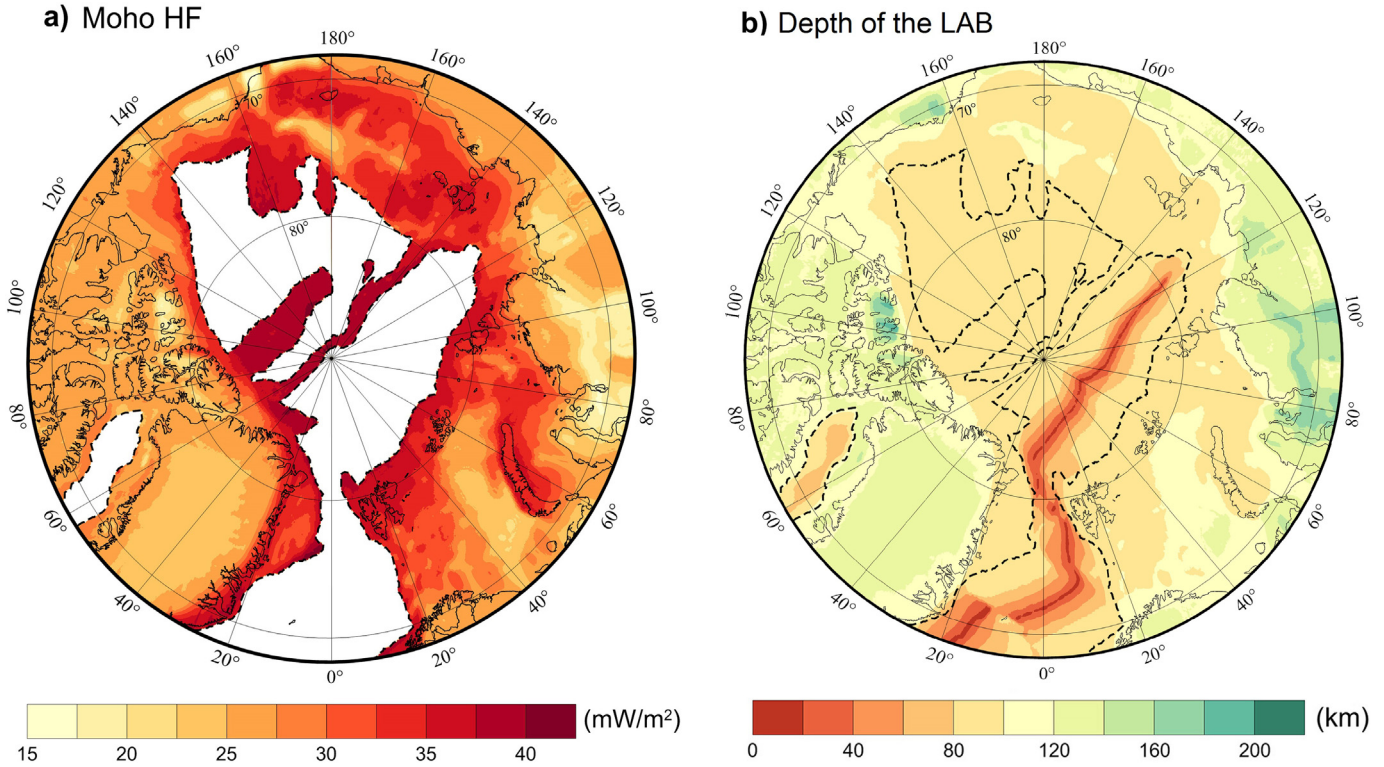

Fig. 8. (a) *HF* at the Moho depth in the continental realm. (b) Depth of the lithosphere-asthenosphere boundary, estimated as a depth of the isotherm 1350 °C.

Basin (Fig. 6a). The surface heat flow is relatively high ($> 55 mW m^{-2}$, Fig. 3) in this basin, despite its age (Lebedeva-Ivanova et al., 2018), and thus the assumptions used in the plate cooling model may not be fully valid in this area. Indeed, magmatic events that occurred in the Amerasia Basin during Late Cretaceous times may have likely reheated it.

At a depth of 100 km, the temperatures already reach 1350 °C, due to the boundary condition required by the plate model ($T = 1350$ °C at $z = 95$ km). In contrast, the ThermoSeismic model shows in the oceanic realm temperatures 100–250 °C lower. In particular, this model estimates temperatures in the Greenland Sea (1200 °C) higher than in the Eurasia Basin (1100 °C). This may be due to the passive character and ultraslow spreading rate (6–10 mm yr^{-1}) of the Gakkel Ridge, which reduces the temperatures in comparison with an "intermediate" spreading rate type of ridge (55–70 mm yr^{-1}). The high temperatures beneath the Greenland Sea may be linked to active mid-ocean ridge spreading processes and the proximity of the Iceland hotspot, with a recent northerly flow, as documented by seismology (Yakovlev et al., 2012) and basalt geochemistry (e.g., Elkins et al., 2016).

In general, we can observe that the differences between the two thermal models likely arise from the different approaches and thus assumptions used to produce them. In particular, the seismic tomography model and its inversion into temperature is affected by uncertainties related to possible undersampling by seismic travel paths and by the lack of knowledge about the possible compositional variations in the upper mantle.

4.2. Strength and effective elastic thickness (Te)

The strength model is displayed in terms of lithospheric integrated strength (Fig. 9a), percentage of crustal contribution (Fig. 9b), and lithospheric variations along the three cross-sections (Fig. 10), located in Fig. 6a. Furthermore, we display coupling/decoupling conditions of lithospheric layers and *Te* in Figs. (11a-116a). It should be noted that these estimates are not direct observations, but the results of a high-resolution crustal model based on gravity data (Lebedeva-Ivanova et al., 2018) and of assumptions, appropriate for the geological conditions of the study area on a large-scale (e.g., average surface heat flow values and crustal rheology used). In particular, *Te* estimates have to be considered an upper bound of the possible values, since the assumptions of a stiff crustal rheology, justified by a widespread mafic crust, promote coupling conditions of the lithospheric layers in almost the entire study area. Obviously, assuming a soft crustal rheology (e.g., wet quartzite for the upper crust and wet diorite for the lower crust) and/or a different crustal division (e.g., an upper crustal thickness equal to 70% of the entire crust) lead to a hotter and weaker lithosphere (Fig. S2). On the other hand, the effects of uncertainties of temperatures, crustal thickness, and rheology on strength and *Te* often counteract each other and are difficult to quantify (e.g., Tesauro et al., 2015; Tesauro et al., 2013, and Tesauro et al., 2012). Therefore, we prefer a qualitative discussion of the results, linking them with the structure of the tectonic features. The on- and offshore regions are characterized by relatively high ($> 1 \times 10^{13}$ Pa m) and low ($< 1 \times 10^{13}$ Pa m) integrated strength (Fig. 9a), respectively, according to the two different input values for surface heat flow (Fig. 3). However, we can notice that the variation from an oceanic to a stretched continental crustal type in the Canada Basin (where in some parts the crustal nature is still uncertain) does not cause any sharp change in the strength and *Te* values, on account of its uniform low thickness. One exception is given by Greenland, where we observe a decrease in the integrated strength from the margins to the inner part to values lower than 1×10^{13} Pa m. This result is not related to significant lateral temperature variations (cross-section A-A', Fig. 7), but to an increase of crustal thickness in its central part (Fig. 1b), which promotes ductile deformation in the lower crust and reduction of strength in the mantle lithosphere (Fig. 10, cross-section A-A'). Different from the North American cratons, where the strength is mainly concentrated in the mantle lithosphere (Tesauro et al., 2015), in Greenland as well as in other cratons of the Arctic region, the strength is primarily localized in the crust (> 70%), due to their relatively high temperatures. However, the large crustal thickness of the area is not sufficient to

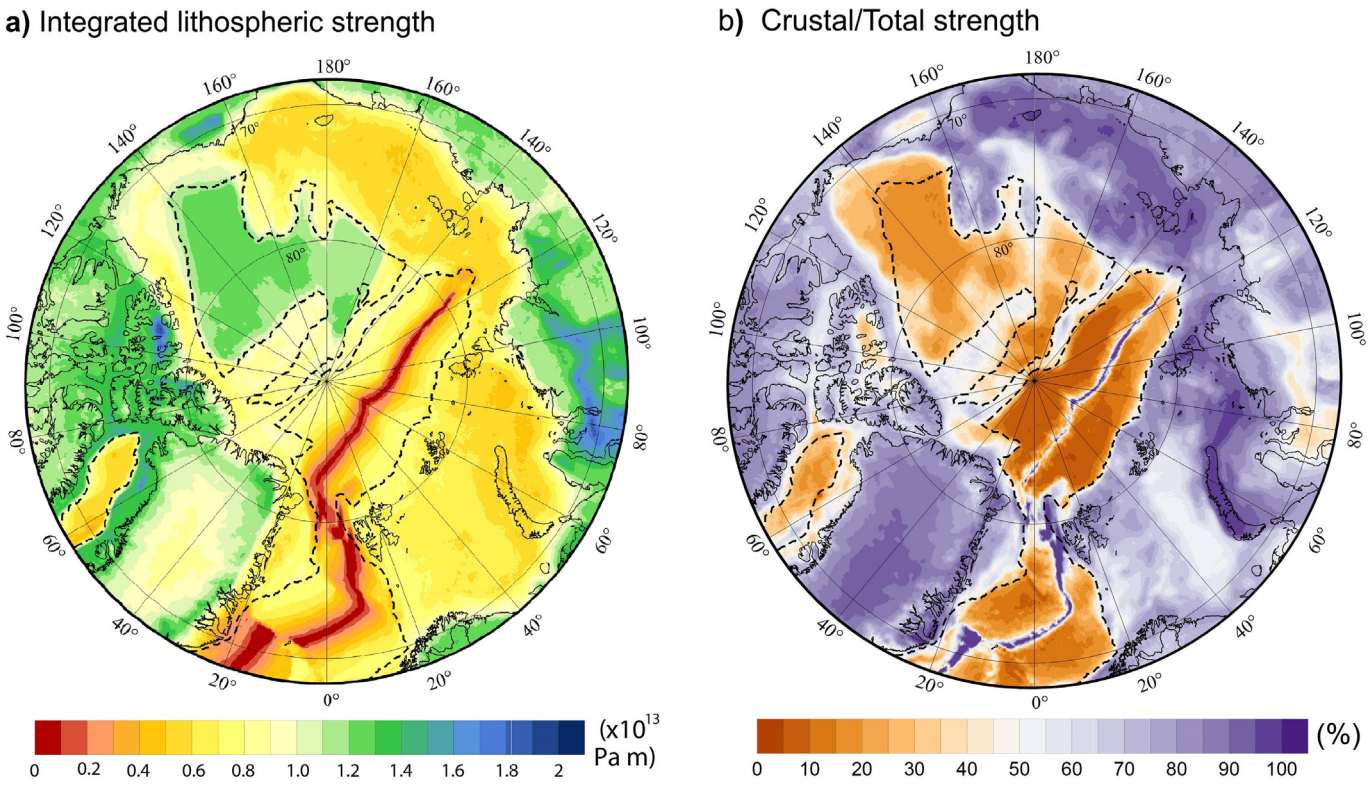

Fig. 9. (a) Integrated lithospheric strength for extension (b); and crustal contribution to the integrated lithospheric strength.

cause decoupling conditions, on account of the low surface heat flow assumed (see Section 3.2.1). In case central-eastern Greenland is thermally perturbed, as predicted by Rogozhina et al. (2016), we would observe crust-mantle lithosphere decoupling, and thus a sharp reduction of *Te* in this area. Other onshore continental regions, such as the Sverdrup Basin and Yenisey Khatanga Basin are characterized by low crustal thickness and temperatures (Fig. 1b, 6a-b). In these areas the strength is mainly residing in the mantle lithosphere (Fig. 10, cross-section C-C′), as indicated by the crustal/lithospheric strength ratio (< 40%, Fig. 9b).

In offshore continental regions with high crustal thickness (> 30 km, Fig. 2b-2c) and high temperatures (~700 °C at 40 km, Fig. 6a, and Fig. 7, Section A-A'), such as the East Siberian Shelf, the strength is almost exclusively concentrated in the crust (> 90%, Fig. 9b). At the same time, the crustal/lithospheric strength ratio decreases to 40–60% (Fig. 9b) in the Barents Sea and even more significantly in the Beaufort Sea (< 30%, Fig. 9b), regions which are characterized by a thin crystalline crust (< 20 km), overlain by a thick sedimentary cover (up to 18 km, 1a), and relative low lithospheric temperatures (500 °C at 40 km, Fig. 6a and Fig. 7 Section B-B′). These conditions lead to the presence of a mechanically strong upper mantle 20–30 km thick (Fig. 10, cross-section B-B′).

We can observe that although at least 50% of the strength is localized in the crust in most of the continental Arctic, all lithospheric layers are coupled (Fig. 11a), and the lithosphere thus deforms as a single plate, similar to oceanic lithosphere. This results in relatively large values of *Te*, which span from 42 to 55 km along the continental shelves, ~ 62–75 km in the cratonic areas of Greenland, Canadian Arctic, and Siberia and values up to ~ 85 km in the Sverdrup and Yenisey Khatanga Basin (Fig. 11b). These estimates indicate that the mantle lithosphere also makes a significant contribution to the *Te* of these features, favoring their long-term stability (e.g., François et al., 2013).

The integrated strength of the oceanic lithosphere (Fig. 9a) ranges from 2.5×10^{10} Pa m along the Mid-Atlantic Ridge to 8×10^{12} Pa m in areas close to the oceanic-continental transition. The largest values of integrated strength are observed in the old Amerasia Basin (1.25×10^{13} Pa m). Along the active mid-oceanic ridge the strength is located only within the thin crust, because of the absence of the mantle lithosphere (Fig. 9b). In contrast, in all other parts of the oceanic domain, the strength is mainly located in the mantle lithosphere (up to > 90%), since its thickness increases fast with cooling, unlike crustal thickness which remains constant (Fig. 9b and Fig. 10, cross-section B-B′). The only oceanic region in which the strength is almost equally partitioned between the crust and upper mantle is the Amerasia Basin, on account of its anomalous thick crust (Fig. 1b). Consequently, in the entire oceanic area the lithospheric layers are coupled (Fig. 11a) and *Te* tends to increase from the ridge (~8 km) towards the ocean-continent transitional areas (~42 km), reaching the largest values (~54 km) in the old Amerasia Basin (Fig. 11b).

4.3. Seismicity, faulting and strength distribution

Earthquakes occur at much faster strain rate (10^{-3}–10^{-6} s^{-1}) than geological stain rates for which the YSE's are computed (10^{-15} s^{-1}). Consequently, the long-term brittle-ductile transition (BDT) depth cannot be considered as a direct proxy to maximum seismic depth. However, since earthquakes take place on pre-existing fractures or faults, they will likely occur within a permanently brittle layer (Burov, 2011). Therefore, there is probably a direct correlation between the depth of the BDT and that of the intraplate earthquakes distribution. In order to investigate this aspect and the relation between strength and seismicity, we selected from the ISC catalog (http://www.isc.ac.uk/iscbulletin/search/catalogue/) 2569 earthquakes that occurred from 1970 to present with a magnitude ≥ 4.0 and a depth ranging between 0 and 50 km (mean ~13.1 km and standard deviation ~8.1 km). We displayed the selected earthquakes on top of the map that shows the depth variations of the brittle-ductile transition of the upper crust (UcBDT) (Fig. 12).

We can first observe that a high concentration of seismic events

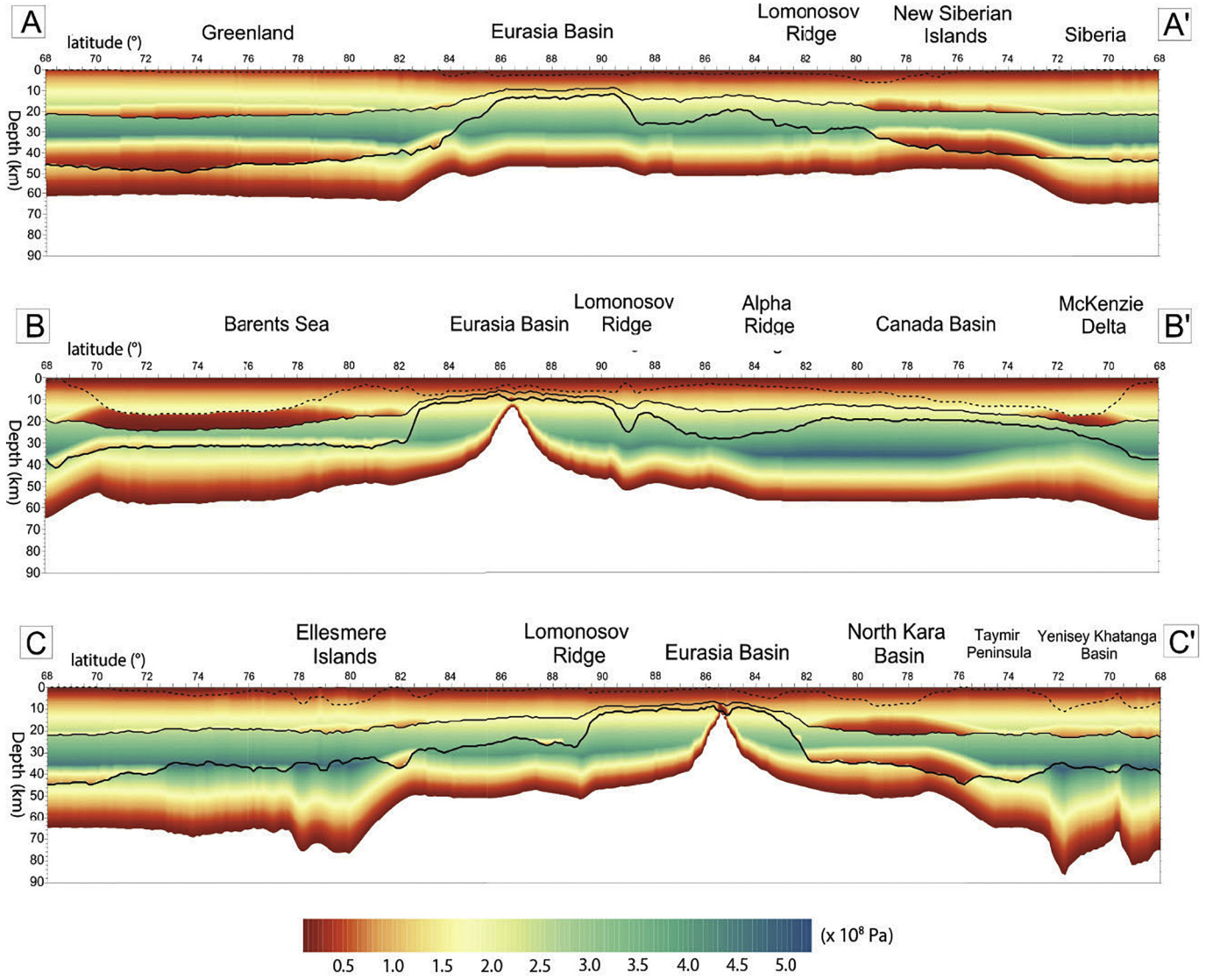

Fig. 10. Lithospheric strength distribution along three cross-sections, displayed in Fig. 6a. Latitudes and depths are displayed along the *x*-axis and *y*-axis, respectively. Continuous thick and dashed black lines show the depth of the Moho and basement, respectively. The thin black line in between shows the upper-lower crust division. White zones, where the strength drops below 10 MPa, represent areas of mechanically decoupling of lithospheric layers.

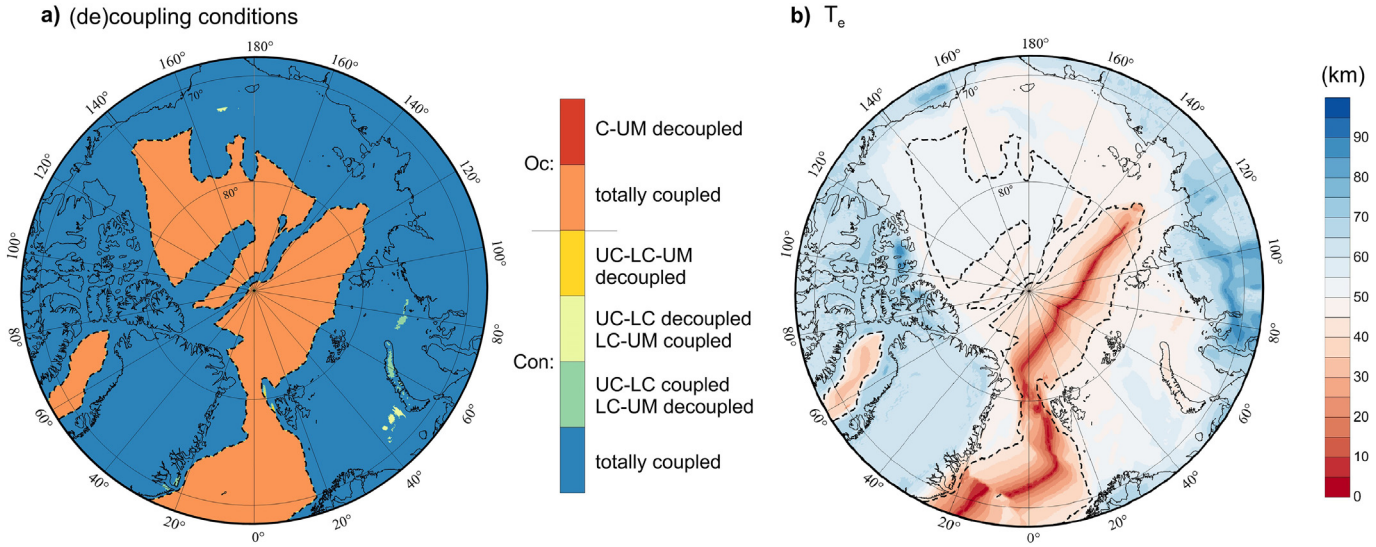

Fig. 11. (a) Coupling and decoupling conditions. (b) Lithospheric variations of the effective elastic thickness (*Te*) for extensional conditions.

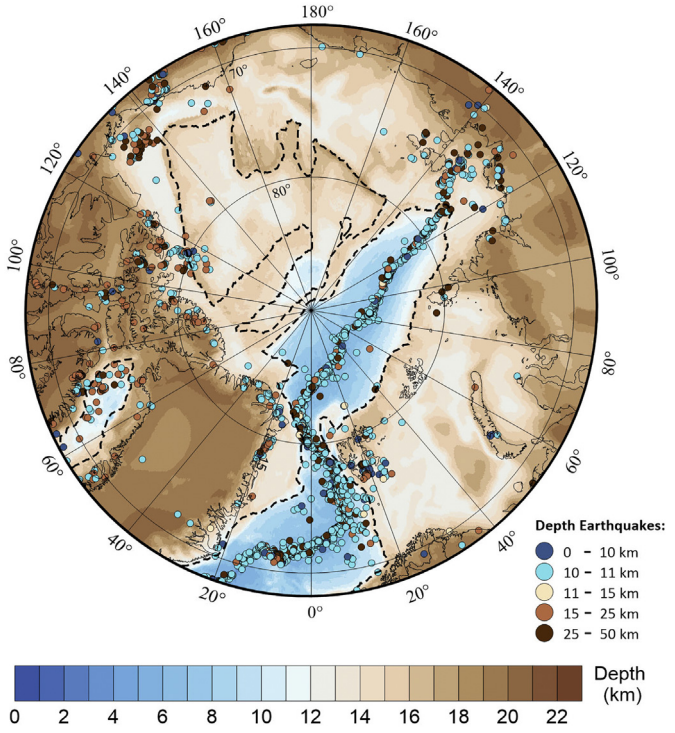

Fig. 12. Depth variations of the brittle-ductile transition in the upper crust (UcBDT). Black curves show the faults in the Arctic region compiled by Doré et al., 2016. Orange and green symbols show the earthquakes (ISC catalog, magnitude ≥4.0) lying below and above the depth of the BDTuc, respectively. In case the upper crust deforms only in a brittle condition, the depth of the BDTuc is replaced by that of the UC. (For interpretation of the references to colour in this figure legend, the reader is referred to the web version of this article.)

exists around the plate boundaries, including the Mid-Atlantic Ridge, the Gakkel Ridge and its prolongation into the Laptev Sea. The number of seismic events in the Greenland Sea is higher than in the Eurasia Basin; this is in agreement with their difference in spreading rates (Dick et al., 2003), since the intensity of magmatic processes, on which the seismic activity depends, is proportional to them (Schlindwein et al., 2007). The major part of these earthquakes occurs at a depth of 10 km (~ 65%) and is located deeper than the depth of the UcBDT, which is very shallow, in view of the extremely thin crust and high temperatures of the area (Fig. 12). Below the UcBDT the high temperatures prevent the storage of the strain energy required to produce an earthquake (Burov, 2011). It should be noted that our strength model may not have a sufficient high vertical resolution to capture small shallowing of the UcBDT, which can likely occur in hot lithosphere near spreading centers. It should be also noted that the depths of the earthquakes have usually relatively large uncertainty (up to 5 km, http://earthquake.usgs.gov/fdsnws/event/1/) and thus can be overestimated along the ridge.

The other seismic events group occur primarily above the depth of the UcBDT, away from tectonically active areas, and are likely due to intraplate stress. In the Greenland Sea we observe clusters of intraplate earthquakes on each basin flank (Fig. 12). In the Baffin Bay, most seismic events are concentrated in the center and western part close to the margins of the Canadian Arctic, where a sharp transition in strength and *Te* is observed (Fig. 9a and 11b). A large number of strong earthquakes occur along the passive margin of North America, also characterized by a sharp lateral variation in strength and *Te*. Previous studies have already found a correlation between intraplate seismicity and the edges of the cratons, where sharp changes of strength and *Te* are observed (Sloan et al., 2011; Tesauro et al., 2015). Note that recent structural and geological data point to a long and narrow zone of deformation that extends from NW Svalbard to northern Alaska (K. Piepjohn, pers. comm., 2017), which was reactivated several times since the Paleozoic and is also active today as indicated by the seismicity trend (Fig. 12).

The hypothesis of a more general correlation between seismic activity and strength/*Te* variations is further supported by the observation that other intraplate continental areas are subjected to extensional stress, but with a more homogeneous distribution of strength and *Te*, such as the Kara and Barents Sea and the Chuckchi and East Siberian Sea, which are essentially aseismic. Furthermore, it should be noted that the earthquakes located along the passive margin of Greenland and Canada may also be triggered by the postglacial rebound that occurred in these areas, as demonstrated by the existing correlation between seismic activity and deglaciated areas (Chung, 2002; Stein et al., 1989; Stewart et al., 2000). These earthquakes are concentrated along the margins of former ice sheets, where different faulting styles (normal, thrust, and strike slip) can be generated, indicating local stress perturbations, induced by glacial unloading (Stewart et al., 2000).

Our results describe the present-day configuration of the Circum-Arctic lithosphere, but most of it has not been drastically modified in recent times. Therefore, we test also possible connections between major faults, which were formed in the geological past, and the depth to the brittle-ductile transition as derived from this study. To this purpose we have chosen the faults' compilation of Doré et al. (2016). Furthermore, thrusting has mainly affected the Arctic during major orogenies, like the Paleozoic Caledonian, Ellesmerian, and Timanian, and the Cenozoic Eurekan orogenies (e.g., Pease et al., 2014). Rifting has occurred along the Arctic Ocean margins since the Mesozoic, and moderate thrusting was accompanied by considerable strike-slip motion north of Greenland in the Paleocene-Eocene Eurekan deformation (e.g., Piepjohn et al., 2016). Prior to the opening of the North Atlantic, extensive rifting took place between Eurasia and Greenland, and this resulted in a plethora of normal faulting. The “major faults” selection (Fig. 12) represents an over-simplification of the fine structure of faulted areas in the continental Arctic domain, but it samples fairly well the faulted Arctic lithosphere. We note that the selected fault locations reside in areas characterized by deep seated BDT (> 15 km), suggesting that these crustal-scale faults are limited to depths of upper to middle crustal level. A number of these faults (in particular those trending parallel to the margins), coincide with the locations of present-day seismicity, localized at the transition between strong cratonic and relatively weak rifted margins lithosphere. In contrast, most of the thrust faults, located more inward in the continental Arctic interiors, are intrinsically aseismic.

5. Conclusions

We present the first comprehensive thermal and strength model of the Arctic lithosphere. The temperature distribution in the continental and oceanic domain has been estimated assuming steady-state conditions and using the plate cooling model of Stein and Stein (1992). The results reveal a first order difference between cold cratonic areas and hot continental shelves. The lowest temperatures are observed in continental regions characterized by a thick sedimentary cover, and thin crystalline crust. The temperatures estimated from the ThermoSeismic model, based on the inversion of the seismic tomography model (Yakovlev et al., 2012), are generally lower than those of the ThermoSteadyState model. In the cratonic areas the ThermoSteadyState model is more consistent with the ThermoSeismic model, because the steady-state conditions are likely more suitable in these regions.

The cratonic areas (Siberia, Scandinavia and the Canadian Arctic) and tectonically active regions (like the plate boundary between the North American and Eurasian plates) are characterized by high and low integrated strength, respectively, according to their thermal structure. At the same time, in Greenland the strength tends to increase from the

margins to the inner part, according to the increase of crustal thickness.

Comparison of the seismicity distribution with the integrated strength, *Te*, and depth of the upper crust BDT variations, indicates that earthquakes are mostly concentrated along the plate boundaries, characterized by areas of weak and thin lithosphere, but also at the zones of sharp lateral changes in strength and *Te*, as at the edges of Greenland and Canadian Artic, where they may reactivate a long-lasting tectonic boundary. In these regions, rebound stress induced by deglaciation may also enhance seismicity.

Supplementary data to this article can be found online at https://doi.org/10.1016/j.gloplacha.2018.07.014.

Acknowledgements

M.S. and M.T. acknowledge the Netherlands Research Centre for Integrated Solid Earth Science (ISES-2016-UU-19), Utrecht University N. L-I. and C.G. acknowledge the support obtained from the Research Council of Norway through its Centers of Excellence funding scheme, project number 223272, and NORRUSS funding scheme, project number 225027. We thank Jeroen Smit for fruitful discussions on Arctic tectonics. We are grateful to Alexander Koptev and an anonymous reviewer for constructive and critical reviews.

References

Afonso, J.C., Ranalli, G., 2004. Crustal and mantle strengths in continental lithosphere: is the jelly sandwich model absolute? Tectonophysics 94, 221–232.
Alvey, A., Gaina, C., Kusznir, N.J., Torsvik, T.H., 2008. Integrated crustal thickness mapping and plate reconstructions for the high Arctic. Earth Planet. Sci. Lett. 274, 310–321.
Artemieva, I.M., 2006. Global 1° × 1° thermal model TC1 for the continental lithosphere: implications for lithosphere secular evolution. Tectonophysics 416, 245–277.
Artemieva, I.M., Mooney, W., 2001. Thermal thickness and evolution of Precambrian lithosphere: a global study. J. Geophys. Res. 106, 16387–16414.
Artemieva, I.M., Thybo, H., 2013. EUNAseis: a seismic model for Moho and crustal structure in Europe, Greenland, and the North Atlantic region. Tectonophysics 609, 97–153. https://doi.org/10.1016/j.tecto.2013.08.004.
Athy, L.F., 1930. Density, porosity and compactation of sedimentary rocks. Bull. Amer. Assoc. Petrol. Geol. 14, 1–24.
Bassin, C., Laske, G., Masters, G., 2000. The current limits of resolution for surface wave tomography in North America. EOS. Trans. Am. Geophys. Un. 81, F897.
Bernstein, S., Kelemen, P.B., Brooks, C.K., 1998. Depleted spinel harzburgite xenoliths in tertiary dykes from East Greenland: Restites from high degree melting. Earth Planet. Sci. Lett. 154, 221–235.
Bernstein, S., Hanghøj, K., Kelemen, P.B., Brooks, C.K., 2006. Ultra-depleted, shallow cratonic mantle beneath West Greenland: dunitic xenoliths from Ubekendt Ejland. Contrib. Mineral. Petrol. 152, 335–347. https://doi.org/10.1007/s00410-006-0109-0.
Brace, W.F., Kohlstedt, D.L., 1980. Limits on lithospheric stress imposed by laboratory experiments. J. Geophys. Res. 85, 6248–6252.
Breivik, A.G., Mjelde, R., Grogan, P., Shimamura, H., Murai, Y., Nishimura, Y., Kuwano, A., 2002. A possible Caledonide arm through the Barents Sea imaged by OBS data. Tectonophysics 355, 67–97.
Brozena, J.M., Childers, V.A., Lawver, L.A., Gahagan, L.M., Forsberg, R., Faleide, J.L., Eldholm, O., 2003. New aerogeophysical study of the Eurasia Basin and Lomonosov ridge: implications for basin development. Geology 31, 825–828.
Burov, E.B., 2011. Rheology and strength of the lithosphere. Mar. Petrol. Geol. 28, 1402–1443.
Burov, E.B., Diament, M., 1995. The effective elastic thickness (Te) of continental lithosphere. What does it really means? J. Geophys. Res. 100, 3895–3904.
Byerlee, J.D., 1978. Friction of rocks. Pure Appl. Geophys. 116, 615–626.
Cammarano, F., Goes, S., Vacher, P., Giardini, D., 2003. Inferring upper-mantle temperatures from seismic velocities. Phys. Earth Planet. Int. 138, 197–222. https://doi.org/10.1016/S0031 9201(03)00156-0.
Carter, N.L., Tsenn, M.C., 1987. Flow properties of continental lithosphere. Tectonophysics 136, 27–63.
Chapman, D.S., 1986. Thermal gradients in the continental crust. In: Dawson, J.B. (Ed.), The Nature of the Lower Continental Crust. 24. Blackwell, pp. 63–70.
Chian, D., Jackson, R., Hutchinson, D.R., Shimeld, J.W., Oakey, G.N., Lebedeva-Ivanova, N., Li, Q., Saltus, R.W., Mosher, D.S., 2016. Distribution of crustal types in the Canada Basin. Arctic Ocean. Tectonophysics. https://doi.org/10.1016/j.tecto.2016.01.038 (in press).
Christensen, N.I., Mooney, W.D., 1995. Seismic velocity structure and composition of the continental crust: a global review. J. Geophys. Res. 100, 9761–9788.
Chung, W., 2002. Earthquakes along the passive margin of Greenland: evidence for postglacial rebound control. Pure Appl. Geophys. 159, 2567–2584.
Cloetingh, S.A.P.L., Haq, B., 2015. Sea level change. Inherited landscapes and sea level change. Science 23;347 (6220), 1258375. https://doi.org/10.1126/science.1258375.
Cloetingh, S.A.P.L., Burov, E., Francois, T., 2013. Thermo-mechanical controls on intra-plate deformation and the role of plume-folding interactions in continental topography. Gondwana Res. 24, 815–837.
Corfu, F., Heim, M., 2013. In new perspectives on the Caledonides of Scandinavia and related areas, geology and U–Pb geochronology of the Espedalen complex, southern Norway, and its position in the Caledonian nappe systems. In: Corfu, F., Gasser, D., Chew, D.M. (Eds.), Geol. Soc., Lond., Spec. Publ..
Davies, J.H., 2013. Global map of solid earth surface heat flow Geochem. Geophys. Geosyst. 14 (10), 4608–4622.
Demouchy, S., Tommasi, A., Boffa-Ballaran, T., Cordier, P., 2013. Low strength of Earth's uppermost mantle inferred from tri-axial deformation experiments on dry olivine crystals. Phys. Earth Planet. Int. 220, 37–49.
Dick, H.J.B., Schouten, J.L., Schouten, H., 2003. An ultraslow-spreading class of ocean ridge. Nature 426, 405–412.
Dietz, R.S., Shumway, G., 1961. Arctic basin geomorphology. Bull. Geol. Soc. Am. 72, 1319–1330.
Domeier, M., 2016. A plate tectonic scenario for the Iapetus and Rheic oceans. Gondwana Research 36, 275–295. https://doi.org/10.1016/j.gr.2015.08.003.
Doré, A.G., Lundin, E.R., Gibbons, A., Sømme, T.O., Tørudbakken, B.O., 2016. Transform margins of the Arctic: a synthesis and re-evaluation. In: Nemčok, M., Rybár, S., Sinha, S.T., Hermeston, S.A., Ledvényiová, L. (Eds.), Transform Margins: Development, Controls and Petroleum Systems. 431. Geological Society, London, Special Publications, pp. 63–94. https://doi.org/10.1144/sp431.8.
Dörr, N., Lisker, F., Clift, P.D., Carter, A., Gee, D.G., Tebenkov, A.M., Spiegel, C., 2012. Late Mesozoic - Cenozoic exhumation history of northern Svalbard and its regional significance: constraints from apatite fission track analysis. Tectonophysics 81–92. https://doi.org/10.1016/j. tecto.2011.10.007.
Døssing, A., Gaina, C., Brozena, 2017. Building and breaking a LIP: an example from the high Arctic. Geophys. Res. Lett. 44 (12), 6011–6019. https://doi.org/10.1002/2016GL072420.
Døssing, A., Hopper, J.R., Olesen, A.V., Rasmussen, T.M., Halpenny, J., 2013. New aerogravity results from the Arctic: Linking the latest Cretaceous–early Cenozoic late kinematics of the North Atlantic and Arctic Ocean. Geochem., Geophys., Geosyst. 14. https://doi.org/10.1002/ggge.20253.
Elkins, L.J., Hamelin, C., Blichert-Toft, J., Scott, S.R., Sims, K.W.W., Yeo, I.A., Devey, C.W., Pedersen, R.B., 2016. North Atlantic hotspot-ridge interaction near Jan Mayen Island, 57 55-67 1606. Geochem. Persp. Let. 2, 55–67. https://doi.org/10.7185/geochemlet.1606.
Evangelatos, J., Mosher, D.C., 2016. Seismic stratigraphy, structure and morphology of Makarov Basin and surrounding regions: tectonic implications. Marine Geology 374, 1–13. https://doi.org/10.1016/j.margeo.2016.01.013.
Evans, B., Goetze, C., 1979. The temperature variation of hardness of olivine and its implication for polycrystalline yield stress. J. Geophys. Res. 84, 5505–5524.
Fahnestock, M., Abdalati, W., Joughin, I., Brozena, J., Gogineni, P., 2001. High geothermal heat flow, basal melt and origin of rapid ice flow in Central Greenland. Science 294, 2338–2342.
Faleide, J.I., Bjørlykke, K., Gabrielsen, R.H., 2015. Geology of the Norwegian Continental Shelf. In: Bjørlykke (Ed.), Petroleum Geoscience: From Sedimentary Environments to Rock Physics, https://doi.org/10.1007/978-3-642-34132-8_25.
Foulger, G.R., Panza, G.F., Artemieva, I.M., Bastow, I.D., Cammarano, F., et al., 2013. Caveats on tomographic images. Terra Nova 25, 259–281.
François, T., Burov, E.B., Meyer, B., Agard, P., 2013. Surface topography as key constraint on thermo-rheological structure of stable cratons. Tectonophysics 602, 106–123.
Franke, D., Hinz, K., Ocken, O., 2001. The Laptev sea rift. Mar. Petrol., Geol. 18, 1083–1127.
Franke, D., Hinz, K., Reichert, C., 2004. Geology of the East Siberian Sea, Russian Arctic, from seismic images: structures, evolution, and implications for the evolution of the Arctic Ocean Basin. J. Geophys. Res. 109, B07106. https://doi.org/10.1029/2003JB002687.
Gaina, C., Werner, S.C., Saltus, R., Maus, S., 2011. Circum-Arctic mapping project: new magnetic and gravity anomaly maps of the Arctic. Geol. Soc. Lond. Mem. 35, 39–48.
Gaina, C., Medvedev, S., Torsvik, T.H., Koulakov, I., Werner, S.C., 2014. 4D Arctic: a glimpse into the structure and evolution of the Arctic in the light of new geophysical maps. Surv. Geophys. 35, 1095–1122.
Goes, S., Govers, R., Vacher, P., 2000. Shallow mantle temperatures under Europe from P and S wave tomography. J. Geophys. Res. 105 (B5), 11,153–11,169. https://doi.org/10.1029/ 1999JB900300.
Goetze, C., Evans, B., 1979. Stress and temperature in the bending lithosphere as constrained by experimental rock mechanics. Geophys. J. R. Astron. Soc. 59, 463–478.
Grantz, A., Hart, P., Childers, V., 2011. Geology and tectonic development of the Amerasia and Canada Basins, Arctic Ocean. In: Spencer, A.M., Embry, A.F., Gautier, D.L., Stoupakova, A.V., Sirensen, K. (Eds.), Arctic Petroleum Geology. Geol. Soc. Lond. Mem Vol. 35. pp. 771–799.
Griffin, W.L., O'Reilly, S.Y., Abe, N., Aulback, S., Davies, R.M., Pearson, N.J., Doyle, B.J., Kivi, K., 2003. The origin and evolution of Archean lithospheric mantle. Precambrian Res. 127, 19–41.
Hantschel, T., Kauerauf, A.I., 2009. Fundamentals of Basin and Petroleum Systems Modeling. Springer, Berlin Heidelberg, Germany (ISBN 978-3540723172).
Hasterok, D., Chapman, D.S., 2011. Heat production and geotherms for the continental lithosphere. Earth Planet. Sci. Lett. 307, 59–70.
Hoffmeister, A.M., 1999. Mantle values of thermal conductivity and the geotherm from phonon lifetimes. Science 283, 1699–1706.
Ivanov, A.V., He, H., Yan, L., Ryabov, V.V., Shevko, A.Y., Palesskii, S.V., Nikolaeva, I.V., 2013. Siberian traps large igneous province: evidence for two flood basalt pulses around the Permo-Triassic boundary and in the middle Triassic, and contemporaneous granitic magmatism. Earth-Science Reviews 122, 58–76. https://doi.

org/10.1016/j.earscirev.2013.04.001.
Jackson, I., Fitz Gerald, J.D., Faul, U.H., Tan, B.H., 2002. Grain-size-sensitive seismic wave attenuation in polycrystalline olivine. J. Geophys. Res. 107 (B12), 2360. https://doi.org/10.1029/2001JB001225.
Jakobsson, M., Mayer, L., Coakley, B., Dowdeswell, JA., Forbes, S., Fridman, B., Hodnesdal, H., Noormets, R., Pedersen, R., Rebesco, M., Schenke, HW., Zarayskaya, Y., Accettella, D., Armstrong, A., Anderson, RM., Bienhoff, P., Camerlenghi, A., Church, I., Edwards, M., Gardner, JV., Hall, JK., Hell, B., Hestvik, O., Kristoffersen, Y., Marcussen, C., Mohammad, R., Mosher, D., Nghiem, SV., Pedrosa, MT., Travaglini, PG., Weatherall, P., 2012. The international bathymetric chart of the Arctic Ocean (IBCAO) version 3.0. Geophys. Res. Lett. 39, L12609.
Jaupart, C., Mareschal, J.C., 1999. The thermal structure and thickness of continental roots. Lithos 48, 93–114.
Johansen, S.E., Ostisty, E., BK, Birkeland, Fedorovsky, O., YF, Martirosjan, VN, Christensen, OB, Cheredeev, Ignatenko, S.I., E. A., And Margulis, L. S., 1993. Barents Sea region: play distribution and potential. Norw. Petr. Soc. Spec. Pub. 2, 273–320.
Jokat, W., Ickrath, M., 2015. Structure of ridges and basins off East Siberia along 81°N, Arctic Ocean. Mar. Petr. Geol. 64, 222–232. https://doi.org/10.1016/j.marpetgeo.2015.02.047.
Kaban, M.K., Tesauro, M., Mooney, W.D., Cloetingh, S.A.P.L., 2014. Density, temperature and composition of the North American lithosphere: new insights from a joint analysis of seismic, gravity and mineral physics data. Part 1. Density structure of the crust and upper mantle. Geochem., Geophys., Geosyst. (G-cubed) 15 (12), 4781–4807. https://doi.org/10.1002/2014GC005483.
Kennett, B.L.N., Engdahl, E.R., Buland, R., 1995. Constraints on seismic velocities in the earth from travel times. Geophys. J. Int. 122, 108–124.
Klitzke, P., Faleide, J.I., Scheck-Wenderoth, M., Sippel, J., 2015. A lithosphere-scale structural model of the Barents Sea and Kara Sea region. Solid Earth 6, 153–172.
Klitzke, P., Sippel, J., Faleide, J.I., Scheck-Wenderoth, M., 2016. A 3D gravity and thermal model for the Barents Sea and Kara Sea. Tectonophysics 684, 131–147. https://doi.org/10.1016/j.tecto.2016.04.033.
Koptev, A.I., Ershov, A.V., 2011. Thermal thickness of the Earth's lithosphere: a numerical model. Andean Geol. 5, 25–32.
Koulakov, I., Tychkov, S., Bushenkova, N., Vasilevskiy, A., 2002. Structure and dynamics of the upper mantle beneath the Alpine–Himalayan orogenic belt from teleseismic tomography. Tectonophysics 358, 77–96.
Kreemer, C., Blewitt, G., Klein, E.C., 2014. A geodetic plate motion and global strain rate model. Geochem. Geophys. Geosyst. 15, 3849–3889. https://doi.org/10.1002/2014GC005407.
Kumar, P., Kind, R., Hanka, W., Wylegalla, K., Reigber, C., Yuan, X., Woelbern, I., Schwintzer, P., Fleming, K., Dahl-Jensen, T., Larsen, T.B., Schweitzer, J., Priestley, K., Gudmundsson, O., Wolf, D., 2005. The lithosphere-asthenosphere boundary in the north-West Atlantic region. Earth Planet. Sci. Lett. 236, 249–257.
Laske, G., Masters, G., Ma, Z., Pasyanos, M., 2013. Update on CRUST1.0 — a 1-degree global model of Earth's crust. Geophys. Res. Abstr. 15 (Abstract EGU2013-2658, 2013).
Lebedeva-Ivanova, N., Gaina, C., Minakov, A., Kashubin, S., 2018. ArcCRUST: Arctic Moho and Crustal Thickness from 3D Gravity Inversion, G3 (Submitted).
Levshin, A.L., Schweitzer, J., Weidle, C., Shapiro, N.M., Ritzwoller, M.H., 2007. Surface wave tomography of the Barents Sea and surrounding regions. Geophys. J. Int. 170, 441–459. https://doi.org/10.1111/j.1365-246X.2006.03285.x.
Maher Jr., H.D., 2001. Manifestation of the cretaceous high Arctic large Igneous Province in Svalbard. J. Geol. 109, 91–104.
McDonough, W.F., Sun, S.-S., 1995. The composition of the earth. Chem. Geol. 120, 223–253.
McKenzie, D.P.J., 1967. Some remarks on heat ow and gravity anomalies. J. Geophys. Res. 72, 6261–6273.
Mei, S., Suzuki, A.M., Kohlstedt, D.L., Dixon, N.A., Durham, W.B., 2010. Experimental constraints on the strength of the lithospheric mantle. J. Geophys. Res. 115, B08204. https://doi.org/10.1029/2009JB006873.
Minakov, A., Faleide, J.I., Glebovsky, V.Y., Mjelde, R., 2012. Structure and evolution of the northern Barents-Kara Sea continental margin from integrated analysis of potential fields, bathymetry and sparse seismic data. Geophys. J. Int. 188, 79–102.
Nikishin, A.M., Malyshev, N.A., Petrov, E.I., 2014. Geological Structure and History of the Arctic Ocean. EAGE Publications, Houten.
Nikishin, Petrov, E.I., Gaina, C., Burov, E.B., Kazmin, Yu, B., Glumov, I.F., Morozov, A.F., Cloetingh, S., Gerya, T., Posamentier, H.W., Ershova, V., Koptev, A., Kulyukina, N.A., Lebedeva-Ivanova, N., 2018. Simultaneous widespread intra-plate normal faulting and ultraslow oceanic spreading in Arctic Ocean. Nature Communications (under review).
O'Regan, M., Preto, P., Strannel, C., Jakobsson, M., Koshurnikov, A., 2016. Surface heat flow measurements from the east Siberian continental slope and southern Lomonosov ridge, Arctic Ocean. Geochem. Geophys. Geosyst. 17. https://doi.org/10.1002/2016GC006284.
Parsons, B., Sclater, J.G., 1977. An analysis of the variation of ocean floor bathymetry and heat ow with age. J. Geophys. Res. 82, 803–827.
Pease, V., Drachev, S., Stephenson, R., Zhanga, X., 2014. Arctic lithosphere - a review. Tectonophysics 628, 1–25.
Petrov, O., Morozovb, A., Shokalskya, S., Kashubina, S., Artemieva, I.M., Soboleva, N., Petrova, E., Ernst, R.E., Sergeeva, S., Smelror, M., 2016. Crustal structure and tectonic model of the Arctic region. Earth Sci. Rev. 154, 29–71.
Piepjohn, K., von Gosen, W., Tessensohn, F., 2016. The Eurekan deformation in the Arctic: an outline: J. Geol. Soc. 22. https://doi.org/10.1144/jgs2016-081.
Pollack, H., Chapman, D.S., 1977. Mantle heat flow. Earth Planet. Sc. Lett. 34, 174–184.
Ranalli, G., 1994. Nonlinear flexure and equivalent mechanical thickness of the lithosphere Tectonophysics 240. pp. 107–114.
Ranalli, G., Adam, M., 2013. Rheological contrast at the continental Moho: effects of composition, temperature, deformation mechanism, and tectonic regime. Tectonophysics 609, 480–490.
Rickers, F., Fichtner, A., Trampert, J., 2013. The Iceland–Jan Mayen plume system and its impact on mantle dynamics in the North Atlantic region: evidence from full-waveform inversion. Earth Planet. Sci. Lett. 367, 39–51.
Ritsema, J., Deuss, A., van Heijst, H., Woodhouse, J.H., 2011. S40RTS: a degree-40 shear-velocity model for the mantle from new Rayleigh wave dispersion, teleseismic traveltime and normal-mode splitting function measurements. Geophys. J. Int. 184 (3), 1223–1236.
Rogozhina, I., Petrunin, A.G., Vaughan, A.P.M., Steinberger, B., Johnson, J.V., Kaban, M.K., Calov, R., Rickers, F., Thomas, M., Koulakov, I., 2016. Melting at the base of the Greenland ice sheet explained by Iceland hotspot history. Nat. Geosci. 9, 366–369.
Rybach, I., Buntebarth, B., 1982. Relationship between the petrophysical properties density seismic velocity, heat generation and mineralogical constitution. Earth Planet. Sci. Lett. 57, 367–376.
Schaeffer, A.J., Lebedev, S., 2013. Global shear-speed structure of the upper mantle and transition zone. Geophys. J. Int. 194, 417–449.
Schlindwein, V., Muller, C., Jokat, W., 2007. Microseismicity of the ultraslow-spreading Gakkel ridge, Arctic Ocean: a pilot study. Geophys. J. Int. 169, 100–112.
Seipold, U., 1992. Depth dependence of thermal transport properties for typical crustal rocks. Phys. Earth Planet. Int. 69, 299–303.
Shapiro, N.M., Ritzwoller, M.H., 2002. Monte-Carlo inversion for a global shear-velocity model of the crust and upper mantle. Geophys. J. Int. 151, 88–105. https://doi.org/10.1046/j.1365- 246X.2002.01742.x.
Shephard, R., Müller, D., Seton, M., 2013. The tectonic evolution of the Arctic since Pangea breakup: integrating constraints from surface geology and geophysics with mantle structure. Earth Sci. Rev. 124, 148–183.
Sloan, R.A., Jackson, J.A., McKenzie, D., Priestley, K., 2011. Earthquake depth distributions in Central Asia, and their relations with lithosphere thickness, shortening and extension. Geophys. J. Int. 185, 1–29.
Smit, J., van Wees, J.D., Cloetingh, S., 2016. The Thor suture zone: from subduction to intraplate basin setting. Geology 44, 707–710. https://doi.org/10.1130/G37958.1.
Smit, J., Van Wees, J.D., Cloetingh, S., 2018. Early carboniferous extension in eastern Avalonia: 350 my record of lithospheric memory. Mar. Pet. Geol. 92, 1010–1027 (in press).
Spasojevic, S., Gurnis, M., 2012. Sea level and vertical motion of continents from dynamic earth models since the late cretaceous. Am. Ass. Petr. Geol. Bull. 96, 2037–2064.
Srivastava, S.P., 1985. Evolution of the Eurasian Basin and its implication to the motion of Greenland along Nares Strait. Tectonophysics 114, 29–53.
Stein, C.A., Stein, S., 1992. A model for the global variation in oceanic depth an heat ow with lithospheric age. Nature 359, 123–129.
Stein, S., Cloetingh, S., Sleep, N.H., Wortel, R., 1989. Passive margin earthquakes, stresses and rheology. In: Gregeren, S., Basham, P.W. (Eds.), Earthquakes at North Atlantic Passive Margins: Neotectonics and Postglacial Rebound. Kluwer Math. Phys. Sciences, NATO ASI Series, pp. 231–259.
Stewart, I.S., Sauber, J., Rose, J., 2000. Glacio-seismotectonics: ice sheets, crustal deformation and seismicity. Quat. Sci. Rev. 19, 1367–1389.
Stixrude, L., Lithgow-Bertelloni, C., 2005. Thermodynamics of mantle minerals – I Physical properties. Geophys. J. Int. 162, 610–632.
Storey, M., Duncan, R.A., Tegner, C., 2007. Timing and duration of volcanism in the North Atlantic Igneous Province: implications for geodynamics and links to the Iceland hotspot. Chem. Geol. 241 (3–4), 264–281.
Tesauro, M., Kaban, M.K., Cloetingh, S.A.P.L., 2009. A new thermal and rheological model of the European lithosphere. Tectonophysics 473, 478–495.
Tesauro, M., Audet, P., Kaban, M.K., Bürgmann, R., Cloetingh, S.A.P.L., 2012. The effective elastic thickness of the continental lithosphere: comparison between rheological and inverse approaches. Geochem. Geophys. Geosyst. 13, Q09001. https://doi.org/10.1029/2012GC004162.
Tesauro, M., Kaban, M.K., Cloetingh, S.A.P.L., 2013. Global model for the lithospheric strength and effective elastic thickness. Tectonophysics 602, 78–86.
Tesauro, M., Kaban, M.K., Mooney, W.D., Cloetingh, S.A.P.L., 2014. Density, temperature and composition of the North American lithosphere: New insights form a joint analysis of seismic, gravity and mineral physics data. Part II: Thermal and compositional model of the upper mantle. Geophys. Geochem. Geosyst. 15, 4808–4830. https://doi.org/10.1002/2014GC005484.
Tesauro, M., Kaban, M.K., Mooney, W.D., 2015. Variations of the lithospheric strength and elastic thickness in North America. Geochem. Geophys. Geosyst. 16, 2197–2220.
Vilà, M., Fernndez, M., Jimenez-Munt, I., 2010. Radiogenic heat production variability of some common lithological groups and its significance to lithospheric thermal modeling. Tectonophysics 490, 152–264.
Wilks, K., Carter, N.L., 1990. Rheology of some continental lower crustal rocks. Tectonophysics 182, 57–77.
Xu, Y., Shankland, T.J., Linhardt, S., Rubie, D.C., Langenhorst, F., Klasinski, K., 2004. Thermal diffusivity and conductivity of olivine, wadsleyite and ringwoodite to 20 GPa and 1373 K. Phys. Earth Planet. Int. 143-144, 321–336.
Yakovlev, A., Bushenkova, N.A., Koulakov, I.Y., Dobretsov, N.L., 2012. Structure of the upper mantle in the Circum-Arctic region from regional seismic tomography. Russ. Geol. Geophys. 53, 963–971.
Yuan, H., Romanowicz, B., 2010. Lithospheric layering in the north American craton. Nature 466, 1063–1068. https://doi.org/10.1038/nature09332.
Zoth, G., Haenel, R., 1988. In: Haenel, R., Rybach, L., Stegena, L. (Eds.), Appendix in Handbook of Terrestrial Heat Flow Density Determination, pp. 449–453.